



# Rapid Accretion State Transitions following the Tidal Disruption Event AT2018fyk

T. Wevers<sup>1,2</sup>, D. R. Pasham<sup>3</sup>, S. van Velzen<sup>4,5,6</sup>, J. C. A. Miller-Jones<sup>7</sup>, P. Uttley<sup>8</sup>, K. C. Gendreau<sup>9</sup>, R. Remillard<sup>3</sup>, Z. Arzoumanian<sup>9</sup>, M. Löwenstein<sup>9</sup>, and A. Chiti<sup>3</sup>

<sup>1</sup>European Southern Observatory, Alonso de Córdova 3107, Vitacura, Santiago, Chile; [twevers@eso.org](mailto:twevers@eso.org)

<sup>2</sup>Institute of Astronomy, University of Cambridge, Madingley Road, CB3 0HA, Cambridge, UK

<sup>3</sup>MIT Kavli Institute for Astrophysics and Space Research, Cambridge, MA 02139, USA

<sup>4</sup>Leiden Observatory, Leiden University, P.O. Box 9513, 2300 RA, Leiden, Netherlands

<sup>5</sup>Center for Cosmology and Particle Physics, New York University, NY 10003, USA

<sup>6</sup>Department of Astronomy, University of Maryland, College Park, MD 20742, USA

<sup>7</sup>ICRAR—Curtin University, GPO Box U1987, Perth, WA 6845, Australia

<sup>8</sup>Anton Pannekoek Institute, University of Amsterdam, Science Park 904, 1098 XH, Amsterdam, Netherlands

<sup>9</sup>Astrophysics Science Division, NASA Goddard Space Flight Center, Greenbelt, MD 20771, USA

Received 2021 January 11; revised 2021 February 27; accepted 2021 March 15; published 2021 May 17

## Abstract

Following a tidal disruption event (TDE), the accretion rate can evolve from quiescent to near-Eddington levels and back over timescales of months to years. This provides a unique opportunity to study the formation and evolution of the accretion flow around supermassive black holes (SMBHs). We present 2 yr of multiwavelength monitoring observations of the TDE AT2018fyk at X-ray, UV, optical, and radio wavelengths. We identify three distinct accretion states and two state transitions between them. These appear remarkably similar to the behavior of stellar-mass black holes in outburst. The X-ray spectral properties show a transition from a soft (thermal-dominated) to a hard (power-law-dominated) spectral state around  $L_{\text{bol}} \sim \text{few} \times 10^{-2} L_{\text{Edd}}$  and the strengthening of the corona over time  $\sim 100\text{--}200$  days after the UV/optical peak. Contemporaneously, the spectral energy distribution (in particular, the UV to X-ray spectral slope  $\alpha_{\text{ox}}$ ) shows a pronounced softening as the outburst progresses. The X-ray timing properties also show a marked change, initially dominated by variability at long ( $> \text{day}$ ) timescales, while a high-frequency ( $\sim 10^{-3}$  Hz) component emerges after the transition into the hard state. At late times ( $\sim 500$  days after peak), a second accretion state transition occurs, from the hard into the quiescent state, as identified by the sudden collapse of the bolometric (X-ray+UV) emission to levels below  $10^{-3.4} L_{\text{Edd}}$ . Our findings illustrate that TDEs can be used to study the scale (in)variance of accretion processes in individual SMBHs. Consequently, they provide a new avenue to study accretion states over seven orders of magnitude in black hole mass, removing limitations inherent to commonly used ensemble studies.

*Unified Astronomy Thesaurus concepts:* [Transient sources \(1851\)](#); [Time domain astronomy \(2109\)](#); [High energy astrophysics \(739\)](#); [Accretion \(14\)](#); [Active galactic nuclei \(16\)](#); [Low-mass x-ray binary stars \(939\)](#)

## 1. Introduction

Stellar-mass black holes (with masses between 5 and 15  $M_{\odot}$ ) can produce outbursts of radiation triggered by a sudden influx of material. The emission from these outbursts encodes critical information about the physics of accretion onto a compact object, nature’s most efficient way to convert mass to energy. Broadly speaking, three accretion states are observed during these outbursts: the quiescent, the soft, and the hard state (Homan & Belloni 2005; Remillard & McClintock 2006). These states are defined by the relative importance of the two main physical components of the inner accretion flow: the accretion disk, and a hot, tenuous plasma known as the corona.

In quiescence and at the start of an outburst, stellar-mass black holes typically produce relatively hard emission (dominated by higher-energy photons). As it nears peak brightness, the emission becomes soft, i.e., dominated by relatively lower energy photons from the accretion disk, with a weak coronal contribution and low X-ray flux variability. This state is referred to as the soft state. As the outburst intensity declines, the emission becomes harder again, dominated by higher-energy X-ray photons from the corona. This hard state is also characterized by large X-ray variability. As the brightness decreases further, these systems return to the quiescent state. This last is poorly understood because the system is intrinsically very faint, but quiescent emission is typically softer than in the hard state. Evolution across states, which represents a

framework to understand the process of accretion onto black holes, is thought to correlate with the overall mass accretion rate, although other factors (e.g., black hole spin, magnetic flux) likely also play an important role.

A long-standing question in compact object accretion physics is whether supermassive black holes (SMBHs; with masses  $\gtrsim$  a few  $\times 10^5 M_{\odot}$ ) undergo the same accretion cycle, i.e., with similar states and mechanisms that trigger transitions between the states. This is interesting because state transitions signal changes to the fundamental physics governing the accretion processes (Abramowicz & Fragile 2013). These include the dominant cooling mechanism, geometry, interplay between the emitting regions, jet formation, and accretion efficiency. A key question is whether and how these mechanisms scale with the black hole mass.

For actively accreting SMBHs or active galactic nuclei (AGNs), large changes in mass accretion rate similar to stellar-mass black hole outbursts are thought to occur on timescales of hundreds to thousands of years. Observations of multiple state transitions in individual AGNs are therefore very rare (McElroy et al. 2016; Parker et al. 2019), and the observed timescales ( $\sim$ tens of years) highlight the uncertainties in our understanding of the mechanism responsible for such state changes. Observational constraints for SMBHs in different accretion states are largely statistical in nature (Merloni et al. 2003; Falcke et al. 2004; McHardy et al. 2006; although some work

on individual systems exists—e.g., Gezari et al. 2017b; Noda & Done 2018; Frederick et al. 2019; Trakhtenbrot et al. 2019), which severely complicates the development of a detailed, holistic theoretical framework.

Tidal disruption events (TDEs) are episodes in which passing stars are ripped apart by tidal forces in the vicinity of SMBHs within distant galaxies (Hills 1975; Rees 1988). They have long been heralded as ideal systems to study accretion states and transitions in SMBHs, as they evolve from a dormant (quiescent) state to a high accretion rate phase and back again, on  $\sim$ year timescales. However, many TDE accretion disks appear to be stable for at least 5–10 yr after disruption (van Velzen et al. 2019). Moreover, only a small fraction of TDEs show persistently bright X-ray emission, without which a direct comparison to X-ray binary (XRB) spectral and timing properties is challenging. As a result, TDEs with multiple state transitions have not yet been found (see Komossa et al. 2004; Maksym et al. 2014; Jonker et al. 2020; Wevers 2020, for work in this regard).

The transient ASASSN-18ul/AT2018fyk was discovered by the All-Sky Automated Survey for Supernovae (Shappee et al. 2014) on 2018 September 8 in the nucleus of a galaxy at a redshift of 0.059 (luminosity distance of 264 Mpc). Based on the blue optical spectrum with broad H and He emission lines, hot ( $T \sim 35,000$  K) UV/optical blackbody emission that does not cool significantly over time, and the lack of AGN-like emission lines, it was classified as a TDE by a black hole with a (independently derived) mass of  $\log_{10}(M_{\text{BH}}) = 7.7 \pm 0.4 M_{\odot}$  (Wevers et al. 2019a; Wevers 2020).

In this manuscript we present an in-depth analysis of both archival and new radio, optical, UV, and X-ray observations of AT2018fyk taken up to 2 yr after the initial discovery. These data provide three key diagnostics to characterize the accretion flow properties following the TDE, which together enable detailed comparison with stellar-mass black holes:

1. The evolution of the UV–X-ray spectral slope  $\alpha_{\text{ox}}$  with bolometric Eddington ratio.
2. The ratio of the power-law spectral component flux to the total emission in X-rays, and the ratio of power-law emission to the total bolometric luminosity (including the accretion disk, soft excess, and corona).
3. Photometric variability properties of the X-ray emission derived from the Swift and XMM-Newton light curves.

Using these diagnostic tools, we investigate the properties of AT2018fyk and find remarkable similarities to the properties of accreting stellar-mass black holes.

Section 2 details the observations and data reduction. We present the results of modeling the host galaxy and TDE spectral energy distributions (SEDs), as well as the X-ray energy spectral and timing analysis in Section 3. The main results are discussed in the framework of accretion state transitions in Section 4, including similarities and differences between stellar-mass and SMBH systems and a comparison between AT2018fyk and AGNs. We summarize our findings in Section 5.

## 2. Observations and Data Reduction

### 2.1. XMM-Newton Stare Observations

AT2018fyk was observed by the XMM-Newton (Jansen et al. 2001) European Photon Imaging Camera (EPIC) on three

occasions. The first observation (obsID: 0831790201; hereafter referred to as XMM1), for a total of 32 ks, was observed shortly after the initial disk transition began (between states A and B) on 2018 December 9 (MJD 58461.75),  $\approx$ 92 days after discovery. The second observation (obsID: 0853980201; XMM2) was performed  $\approx$ 413 days after discovery (in state D), for a total of 54 ks on 2019 October 26 (MJD 58782.21). The third observation, totaling 17 ks (obsID: 0854591401; XMM3), was taken on 2020 May 12 (MJD 58981.27), roughly 612 days after optical discovery and after the second state transition (in state E). In all the observations EPIC was operating in the imaging mode and the source did not suffer from pileup.<sup>10</sup>

We visually inspect the EPIC (pn+MOS) images from all three observations. A point source coincident with the optical position ( $\alpha = 22:50:16.090$ ,  $\delta = -44:51:53.50$ ; Wevers et al. 2019a) is present in both XMM1 and XMM2 images. However, no source is visible in the X-ray image of XMM3.

We start our data reduction with the raw Observation Data Files and process them using the XMM-Newton Standard Analysis System (SAS) version 17.0.0 tools `epproc` and `emproc`. Using the most recent version of the calibration database (CALDB) files, this procedure results in “cleaned” event files, which are used for deriving scientific products. We extract good time intervals (GTIs) for each of the three observations by screening for periods of background flaring and considering only times when all detectors (pn+MOS1 +MOS2) are active.

Source events are extracted from a circular aperture of radius  $33''$ , which corresponds to roughly 90% of light as estimated from the encircled energy function of the EPIC instruments. For each observation, background events are extracted from two circular regions of radius  $50''$  close to the source and on the same CCD. The energy spectra and light curves are corrected for the different source and background areas. Standard data filters of ( $PATTERN \leq 4$ ) and ( $PATTERN \leq 12$ ) are applied for the pn and MOS data, respectively; we only use events in the 0.3–10 keV band for further analysis. Corresponding response files were generated using XMM SAS tools `rmfgen` and `arfgen`.

For the XMM3 observation, we estimate the X-ray flux upper limit ( $3\sigma$ ) using the EPIC/pn data by following the SAS documentation.<sup>11</sup> Background flaring during XMM3 reduced the effective exposure from 17 ks to about 10 ks. Running the XMMSAS tool `edetect_chain` on a 0.3–10 keV pn image does not yield a point source at the location of AT2018fyk. We estimate the 0.3–10 keV count rate upper limit at the source location to be  $0.0065 \text{ counts s}^{-1}$  using the sensitivity map generated by the `edetect_chain` task. We then use the `fakeit` tool in the X-ray spectral fitting program XSPEC (Arnaud 1996) and the XMM-Newton response files generated using the `arfgen` and `rmfgen` commands to estimate the flux upper limit. Because no constraints on the X-ray spectral shape are available, we estimate the upper limit using the best-fit spectral model parameters from XMM1 and XMM2 with mean 0.3–10 keV count rates of 0.87 and 1.13  $\text{counts s}^{-1}$ , respectively (see Table 4). Assuming that the flux scales linearly in an energy-independent manner, 0.3–10 (0.01–10) keV  $3\sigma$  upper limits are  $8.4 \times 10^{-15}$  ( $7.8 \times 10^{-14}$ )  $\text{erg cm}^{-2} \text{ s}^{-1}$  and  $1.2 \times 10^{-14}$  ( $2.2 \times 10^{-14}$ )  $\text{erg cm}^{-2} \text{ s}^{-1}$  for XMM1

<sup>10</sup> <https://heasarc.gsfc.nasa.gov/docs/xmm/sas/USG/epicpileup.html>

<sup>11</sup> <https://www.cosmos.esa.int/web/xmm-newton/sas-thread-src-find>

and XMM2, respectively. We adopt the more conservative estimates of the XMM2 spectral model in our analysis.

## 2.2. Chandra Stare Observation

Following the nondetection in the latest XMM-Newton exposure (XMM3), we obtained a deep Chandra/ACIS-S Director’s Discretionary Time (DDT) observation. The 46.8 ks exposure started 660 days after the optical discovery (MJD 59029.22). For better sensitivity at low energies, we used the back-illuminated S3 chip in timed exposure mode with the telemetry set to very faint format. Similar to the XMM-Newton/EPIC data reduction, we start our ACIS analysis with the level-1 (secondary) data files, which we reprocess using the Chandra data analysis software (CIAO v4.10). We reduce the level-1 data with the `chandra_repro` script with default parameter values.

We analyze the level-2 event files by first extracting a broadband (0.5–7 keV) X-ray image of the field of view. We use the `fluximage` task with a *bin size* of 1 (0″.492). Visual inspection of the resulting exposure-corrected image does not show a source at the optical position of AT2018fyk. Assuming Poisson statistics and using the CIAO task `srcflux`, we estimate the 0.3–10 keV flux upper limit using the best-fit `bremss+pow` model parameters from XMM1 and XMM2. Both model parameters give a similar value for the unabsorbed  $3\sigma$  flux upper limit in the 0.3–10 keV energy range of  $2 \times 10^{-15} \text{ erg cm}^{-2} \text{ s}^{-1}$ .

## 2.3. NICER Monitoring Observations

The NICER (Gendreau et al. 2016) X-ray Timing Instrument (XTI) on board the International Space Station (ISS) began monitoring AT2018fyk on MJD 58388.15; 242 observations were made with individual exposures lasting between a few tens of seconds and 2000 s. We consider all publicly available observations taken before 2020 January 13 (MJD 58861.34; up to obsID 2200370264). These data are processed using the standard NICER Data Analysis Software (NICERDAS) task `nicerl2` with default filtering and the gain file `nixtflight-pi20170601v004.fits`. Consecutive observations are combined to ensure a minimum of 20 ks of cleaned exposure. This yields a total of 31 energy spectra over the entire monitoring period.

All source spectra are extracted, and background spectra are estimated, as follows. Two empirical background spectrum libraries are constructed from observations of source-free areas of the sky. These include the cosmic X-ray (astrophysical) background associated with those fields, as well as the NICER/XTI instrumental non-X-ray background (NXB). The ISS night background library spectra are collected and categorized into discrete cells according to two background proxies. The first is the count rate of focused events in the 15–18 keV band, where the low effective area of the NICER optics assures that these are not X-rays from the source. The second is the rate of spatially extended (with respect to where X-rays are focused on the detector) events, as identified by their location in the plane of energy versus pulse invariant (PI) ratio of slow chain to fast chain detected events. These are the so-called “trumpet” rejected events.<sup>12</sup> Corresponding rates in the source data are extracted using the input cleaned event file GTIs, subdivided into intervals no larger than 120 s, and a match to one of the background library cells is identified. The total night

background is calculated as a sum over the night library spectra, appropriately weighted by fractional exposure and scaled by the 15–18 keV count rate in each interval relative to the average value in the cell. A supplemental ISS day residual background library is constructed from the same source-free observation database to account for an additional background associated with an optical light leak. This is used to derive an additional background component identified and scaled according to the rate in the 0–0.25 keV energy band.

The total spectrum extracted from the input event list is based on these subdivided GTIs, with the additional excision of data in intervals with background proxies that lie outside of the background library bounds. Also, subdivided GTIs where the absolute value of the estimated net 13–15 keV count rate exceeds  $0.1 \text{ counts s}^{-1}$ , or the estimated background rate exceeds the total rate, are excluded. Data from noisy Focal Plane Modules 14 and 34 are filtered out as well.

## 2.4. Swift Monitoring Observations

Swift started monitoring AT2018fyk on MJD 58383.69, just 2 weeks after its discovery. Between MJD 58383.69 and MJD 59031.24 a total of 161 snapshots were made, which accumulated 198 ks of exposure. All these observations were performed as part of multiple Target of Opportunity (ToO) requests over the ~650-day period. All the data used here are publicly available and can be downloaded from NASA’s High Energy Astrophysics Science Archive (HEASARC).

To measure the UV and optical photometry, a circular aperture of 7″ is used on images taken by the Swift UV and Optical Telescope (UVOT; Roming et al. 2005). We use the task `uvotsource` of HEASOFT v6.24. Subexposures of a given observation are combined before extracting the flux.

For the X-ray Telescope (XRT) data, we start our analysis with the raw level-1 data. These are reduced using `xrtpipeline` with the source optical coordinates. We only use data taken in photon counting mode with event grades between 0 and 12. Source events are extracted from a circular region with a radius of 47″. This value corresponds to roughly 90% (at 1.5 keV) of the light from a point source (as estimated from the XRT fractional encircled energy function). Background events are extracted from an annular region with inner and outer radii of 70″ and 150″, respectively. These values were chosen to avoid point sources in the background annulus. Spectra are binned to a minimum of 20 counts per bin for spectral analysis.

X-ray light curves are then extracted using the `xrtlccorr` task, which properly takes bad pixels and columns into account. For each exposure we estimate the source and background count rates separately. Finally, background-corrected source rates are estimated by subtracting the area-scaled background rates from the source rates. These steps are repeated for both the soft (0.3–1.5 keV) and the hard (1.5–10 keV) X-ray bands to extract the soft and the hard X-ray light curves.

To obtain a deeper constraint on the late-time X-ray emission with Swift, we combine the individual exposures ranging from MJD 58930 to MJD 58975. A  $3\sigma$  upper limit is derived on the combined image, taking into account the combined exposure map, using the `sosta` task in `ximage`. The light-curve data on a per obsID basis can be retrieved from the supplementary files available on Zenodo (`XRT_lightcurve_30_150.dat` and `XRT_lightcurve_150_1000.dat`, doi:10.5281/zenodo.4646229).

<sup>12</sup> [https://heasarc.gsfc.nasa.gov/docs/nicer/mission\\_guide/](https://heasarc.gsfc.nasa.gov/docs/nicer/mission_guide/)

**Table 1**  
ATCA Observations of AT2018fyk

State	MJD (days)	Phase (MJD -58369)	On-source Time (minutes)	Config.	$3\sigma$ Limit ( $\mu\text{Jy beam}^{-1}$ )	$L_{\text{radio}}$ ( $\text{erg s}^{-1}$ )
C	58594.14	225	63	750C	<104	$<6.3 \times 10^{37}$
C	58646.99	278	187	6A	<27	$<1.6 \times 10^{37}$
E	58952.20	583	145	6A	<46	$<2.8 \times 10^{37}$

**Note.** States are labeled as in Figure 4. Upper limits are reported for the stacked image made from the joint deconvolution of the 5.5 and 9.0 GHz data. The corresponding luminosity upper limits are calculated assuming a central frequency of 7.25 GHz.

### 2.5. Australia Telescope Compact Array Observations

Radio observations were obtained with the Australia Telescope Compact Array (ATCA). Observations were performed at early times (25, 52, and 89 days after discovery; see Wevers et al. 2019a for details of these observations), as well as at late times (225, 278, and 583 days after discovery), as detailed in Table 1. For the new late-time observations, we observed in the 4 cm band to maximize sensitivity, with 2 GHz of bandwidth in each of two frequency bands centered at 5.5 and 9.0 GHz. We used the standard calibrator source PKS 1934–638 to determine the bandpass solutions and to set the amplitude scale. We used the nearby calibrator source J2230–4416 to determine the complex gain solutions, which were interpolated onto the target. Data were reduced using the Common Astronomy Software Application (CASA; McMullin et al. 2007). AT2018fyk was not detected in either frequency band at any of the three late-time epochs, and we jointly deconvolved the data from both frequency bands to get the deepest possible upper limits on the source flux density, as reported in Table 1.

## 3. Analysis and Results

### 3.1. Host Galaxy SED Modeling

To estimate the host galaxy brightness in the Swift/UVOT bands, we follow the approach of van Velzen et al. (2021). We use the flexible stellar population synthesis code (Conroy et al. 2009) and pre-flare host galaxy photometry, including UV (GALEX), optical (DeCaLS; Dey et al. 2019), and IR (WISE; Wright et al. 2010) observations to model the SED (see Table 2). The GALEX flux is extracted using the gPhoton software (Million et al. 2016), using the same aperture ( $7''$ ) as applied to the UVOT images. For the WISE photometry we adopt the forced photometry values measured by the Legacy survey (Dey et al. 2019).

Markov Chain Monte Carlo samples of the posterior distribution are used to constrain the model parameters: stellar mass, stellar population age, metallicity, star formation history  $e$ -folding time, and the optical depth of the dust (following the extinction law of Calzetti et al. 2000). The best-fit SED model (Figure 1) is used to synthesize host galaxy magnitudes, which are subsequently subtracted from the measured photometry. The uncertainty on the host flux is propagated into the uncertainty on this difference photometry.

### 3.2. UV/Optical Blackbody Analysis

The UV/optical emission of TDEs can be well described as thermal blackbody emission (van Velzen et al. 2011; Hung et al. 2017). We therefore measure the blackbody temperature

**Table 2**  
Measurements of the Host Galaxy Brightness in UV, Optical, and IR Filters, Used to Model the Host SED

Filter	Measured Magnitude (mag)	Model Magnitude (mag)
GALEX FUV	$23.17 \pm 0.24$	$23.26 \pm 0.25$
GALEX NUV	$22.15 \pm 0.15$	$21.78 \pm 0.15$
DeCaLS $g$	$17.10 \pm 0.04$	$16.94 \pm 0.03$
DeCaLS $r$	$16.34 \pm 0.03$	$16.27 \pm 0.03$
DeCaLS $z$	$15.70 \pm 0.03$	$15.66 \pm 0.03$
WISE W1	$16.00 \pm 0.03$	$16.15 \pm 0.04$
WISE W2	$16.61 \pm 0.04$	$16.81 \pm 0.04$
WISE W3	$16.9 \pm 0.5$	$17.0 \pm 0.5$
Swift UVW2	...	$21.98 \pm 0.10$
Swift UVM2	...	$22.00 \pm 0.15$
Swift UVW1	...	$20.56 \pm 0.08$
Swift $U$	...	$18.80 \pm 0.05$
Swift $B$	...	$17.38 \pm 0.04$
Swift $V$	...	$16.60 \pm 0.03$

**Note.** The model predictions are also presented. Apertures are matched ( $7''$ ) for consistency.

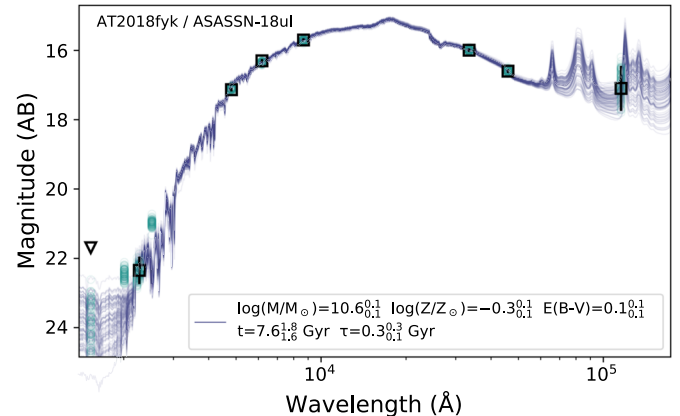


**Figure 1.** Samples from the posterior distribution of host galaxy SED models. The open squares (and triangle) show detections (and one upper limit) from GALEX, DeCaLS, and WISE. Open circles show the synthetic host galaxy magnitude, including predictions for the three bluest bands of the Swift/UVOT instrument.

and luminosity by fitting an evolving temperature blackbody model to the light curve. This also yields the blackbody radius, assuming isotropic emission. To smooth out variations induced by poorly constrained measurements, we use a 40-day smoothing length for the temperature measurements and a 20-day window for the luminosity. Values are linearly interpolated in between grid points.

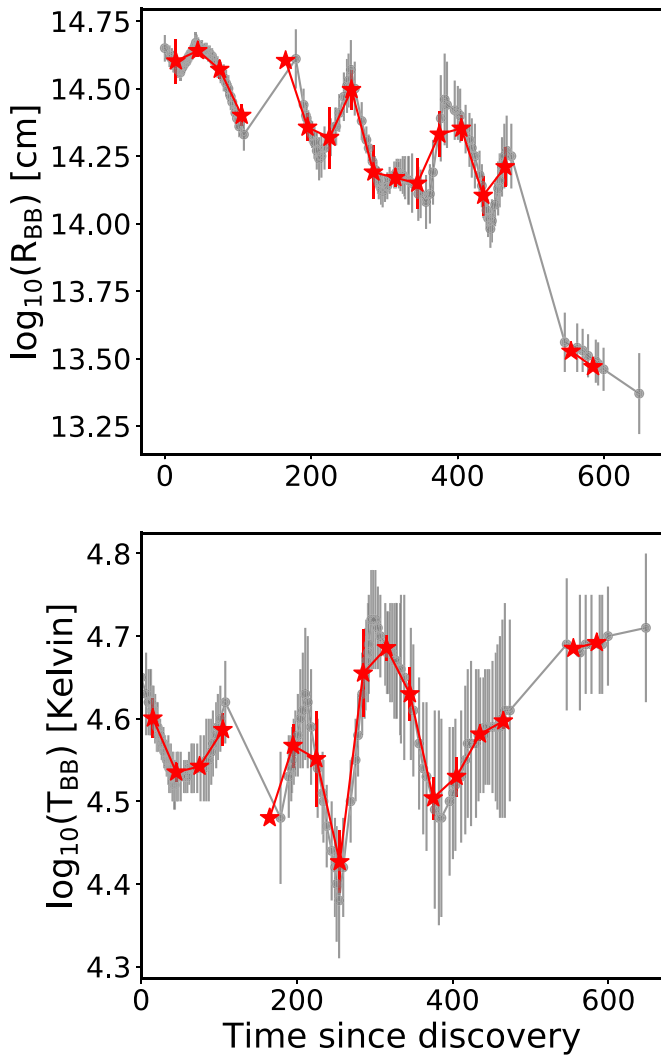


**Figure 2.** Evolution of the blackbody radius (top panel) and temperature (bottom panel) over time. We show the full time resolution measurements (gray), as well as estimates corresponding to the binned data (red). Data to reproduce this figure are available on Zenodo (doi:10.5281/zenodo.4646229).

The blackbody radius and temperature evolution are shown in Figure 2. Individual epoch measurements are shown in gray; binned values are shown in red. The long-term behavior of the radius evolves slowly (decreasing only by a factor of  $\sim 2$ ) up to 450 days. Similarly, the temperature does not cool significantly over the entire light curve, with variations within the error budget. This is somewhat atypical of other TDEs, although there are sources that show a similar evolution (van Velzen et al. 2021). We do note that during the soft state there is some temperature evolution consistent with an  $L \propto T^4$  behavior (Figure 3). At very late times (560 days after discovery) we find that the radius has decreased significantly, while the temperature (although relatively uncertain) does not show any evidence for significant change.

We interpret this lack of significant temperature and radius evolution during the first 500 days as suggestive evidence that the UV emission originates in a stable, rapidly formed accretion disk. At late times, the luminosity decreases significantly, leading to the inferred decrease in radius.

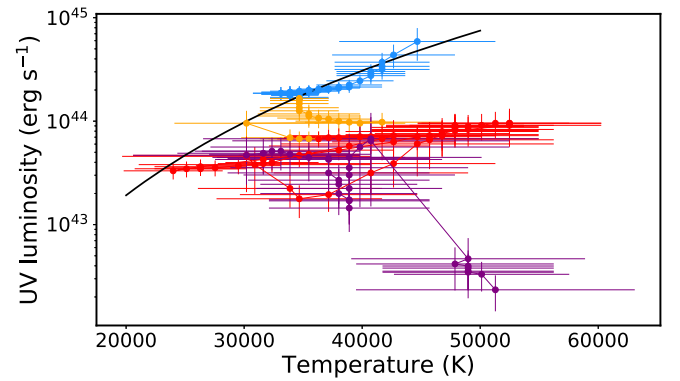


**Figure 3.** TDE UV luminosity as a function of blackbody temperature. The black solid line shows  $L \propto T^4$  behavior (with arbitrary normalization), which describes the behavior in the soft state (A; blue markers) well. The different states are colored according to Figure 4. Data to reproduce this figure are available on Zenodo (doi:10.5281/zenodo.4646229).

### 3.3. The UV–X-Ray Spectral Slope $\alpha_{\text{ox}}$ and Bolometric Eddington Fraction

To probe the broadband long-term evolution of the accretion flow, we employ the UV to X-ray spectral index  $\alpha_{\text{ox}}$  (Tananbaum et al. 1979):

$$\alpha_{\text{ox}} = 1 - \frac{\log_{10}(\lambda L_{2500}) - \log_{10}(\lambda L_{2 \text{ keV}})}{\log_{10}(\nu_{2500}) - \log_{10}(\nu_{2 \text{ keV}})}, \quad (1)$$

where  $\lambda L_{2500}$  and  $\lambda L_{2 \text{ keV}}$  are the monochromatic luminosities at 2500 Å and 2 keV, respectively, and  $\nu_{2500}$  and  $\nu_{2 \text{ keV}}$  are the frequencies at those wavelengths. We use the Swift *UVW1* host-subtracted luminosities ( $\lambda_{\text{cen}} = 2629$  Å) as a proxy for  $L_{2500}$ . These data are included as supplementary data files on Zenodo (doi:10.5281/zenodo.4646229). Based on the observed behavior of  $\alpha_{\text{ox}}$  with bolometric Eddington ratio (Figure 4, top right panel), we divide the TDE evolution into five phases (A through E). These phases are defined based on a combination of  $\alpha_{\text{ox}}$ , X-ray spectral and timing properties, and X-ray and UV variability properties. We summarize the observational properties for each phase in Table 3, but we defer a detailed discussion to Section 4.

The UV blackbody temperature does not cool significantly over the 650-day light curve, with an average temperature of  $T \sim 35,000$  K. The *UVW1* filter is on the Rayleigh–Jeans tail of the blackbody spectrum with  $\log_{10}(T) = 4.63$  K. Similar to van Velzen et al. (2019), we apply a temperature correction to convert the observed luminosity  $L_{\text{UVW1}}$  to a bolometric UV luminosity estimate  $L_{\text{UV}}$ , integrated from 0.03 to 3  $\mu\text{m}$ . This correction amounts to a factor of  $\sim 6.1$ , which is adopted for the entire light curve because of the lack of temperature evolution. We further include the integrated X-ray emission in the 0.01–10 keV energy range (including the EUV band) by extrapolating the spectral model from the observed band to define the bolometric Eddington fraction of emission  $f_{\text{Edd, bol}} \equiv (L_{0.01-10 \text{ keV}} + L_{\text{UV}})/L_{\text{Edd}}$ . A high value of  $\alpha_{\text{ox}}$  indicates a UV (disk) dominated system (also dubbed a soft state), while a low value of  $\alpha_{\text{ox}}$  indicates that the X-ray (corona) emission dominates the energy output (i.e., a hard state).

We use the spectral fits (Section 3.4) to determine the monochromatic 2 keV X-ray flux  $L_{2 \text{ keV}}$ . Given the observed

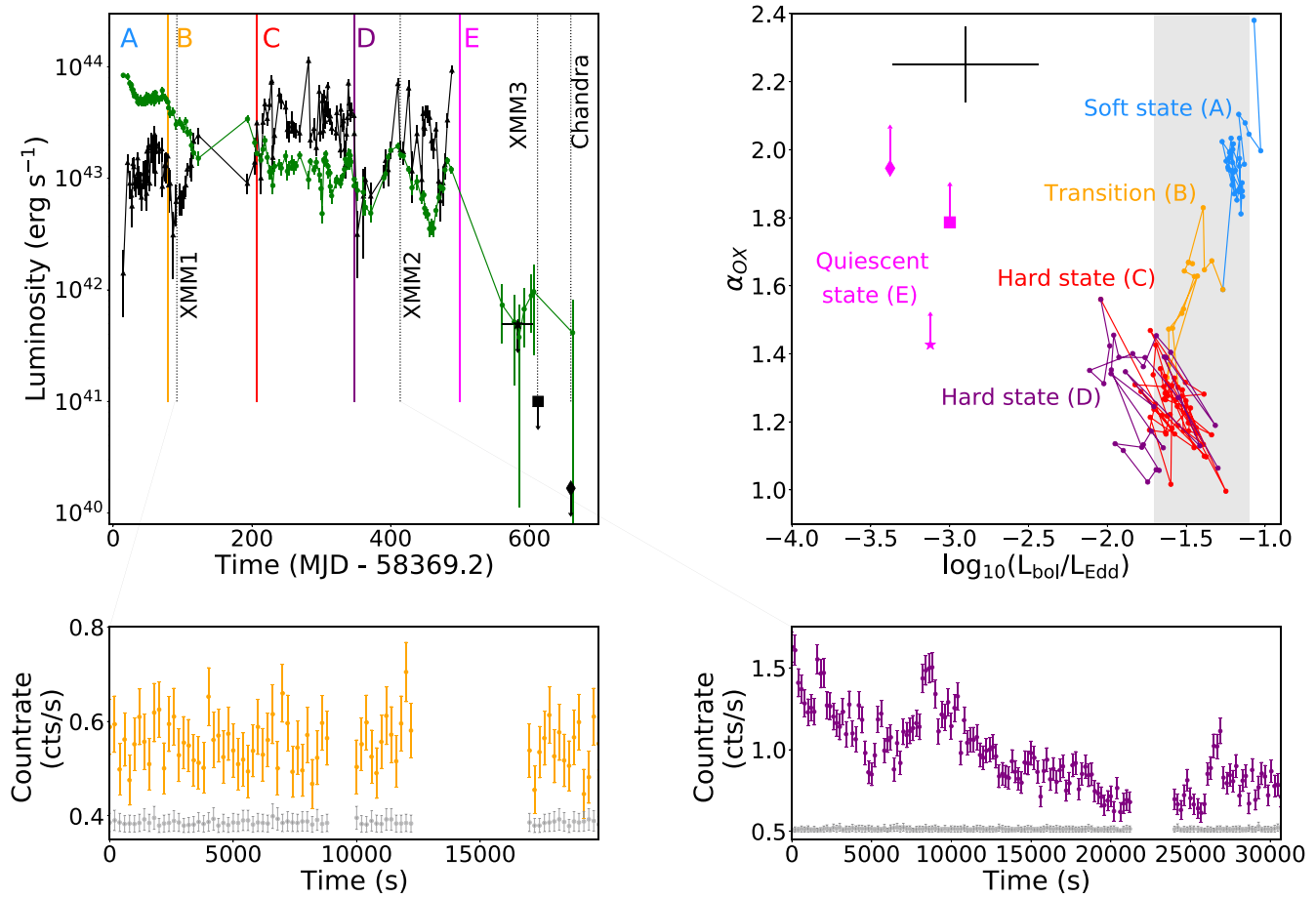


**Figure 4.** Light curves and  $\alpha_{\text{ox}}$  evolution of AT2018fyk. Top left: Swift/XRT 0.3–10 keV (black triangles) and Swift/UVW1 (green circles) light curves. The black star, square, and diamond represent Swift, XMM3, and Chandra X-ray upper limits, respectively. The vertical colored lines denote transitions in source properties as detailed in Section 3.3 and Table 3, while vertical black dashed lines indicate long stare X-ray observations. Top right:  $\alpha_{\text{ox}}$  as a function of the bolometric Eddington fraction. A representative error bar is shown in black in the top left; the uncertainty in  $f_{\text{Edd,bol}}$  is dominated by the intrinsic scatter in the  $M$ - $\sigma$  relation. The typical transition luminosity of stellar-mass black holes is shown as a gray shaded band. Bottom panels: XMM high-cadence (bin size of 200 s) light curves during the XMM1 (left) and XMM2 (right) observations. Background rates are shown in gray, offset (for display purposes) by +0.4 and +0.5 for XMM1 and XMM2, respectively. Data to reproduce this figure are available on Zenodo (doi:10.5281/zenodo.4646229).

spectral variability with time, we use a spectral model for each of the states A (soft), B (transition), and C + D (hard) and take the best-fit power-law index and the appropriate power-law fraction to compute  $L_{2 \text{ keV}}$  for each epoch (Table 4). Because the temperature of the thermal X-ray component is low, the power law dominates the X-ray flux  $> 1.5$  keV at all times, and we ignore the thermal contribution in our estimate of  $L_{2 \text{ keV}}$  (i.e., we only consider the power-law component). Uncertainties are propagated using the standard rules.

We note that in the final epoch of Swift UV observations the *UVM2* brightness is consistent with the SED model prediction for the host galaxy (Table 2). The *UVW1* and *UVW2* magnitudes are still slightly elevated when compared to the prediction for the host galaxy. This could suggest that the SED model magnitudes are slight underestimates of the true host brightness. We assess the impact of this difference, in particular for the *UVW1* filter, by repeating all calculations while assuming a host galaxy brightness equal to that of the last Swift *UVW1* observation, rather than that of the best-fit SED model. The impact on both  $\alpha_{\text{ox}}$  and  $f_{\text{Edd,bol}}$  is small, with changes of up to  $\approx 0.15$  and 0.05, respectively, which does not influence the main conclusions of our work.

The left panel of Figure 4 shows the light curves that were used to compute  $\alpha_{\text{ox}}$  and  $f_{\text{Edd,bol}}$ ; note that epochs with only an

X-ray or *UVW1* measurement are discarded. The source spends approximately 65 days in state A, 125 days in state B (although this is an upper limit owing to a lack of observations in a seasonal gap), and  $\sim 280$  days in the hard state (C and D) afterward. States C and D are spectrally identical in X-rays, but the latter is characterized by large-amplitude variations in the UV band. At very late times (state E), the UV luminosity decreases by a factor of  $\sim 15$ , while the X-ray flux drops by a factor of  $> 5000$  compared to the last detection with Swift. The right panel shows the corresponding behavior in  $\alpha_{\text{ox}}$  and  $f_{\text{Edd,bol}}$ .

### 3.4. X-Ray Spectral Analysis

#### 3.4.1. X-Ray Spectral State Transition

We employ a two-component phenomenological spectral model to characterize the X-ray spectral evolution following the TDE. We use the 0.3–10 keV band, unless stated otherwise. Our focus is on the evolution of the relative strengths of these two model components during the different phases of the TDE. We start our analysis with the XMM1 and XMM2 EPIC/pn spectra, which contain  $\approx 12,000$  and 28,000 counts for the early and late epochs, respectively. We also tabulate the results of the spectral fitting of the XRT stacked spectra (Table 4) and

**Table 3**  
Observational Properties for Each Phase Labeled in Figure 4

Phase/State	MJD	Phase	$\alpha_{\text{ox}}$	$f_{\text{Edd}}$	X-ray Spectral State	X-ray PSD Power	UV Var.
A/Soft	58383–58446	14–77	2.0	$\sim 0.1$	BB dominated	Low $\nu$ ( $< 10^{-5}$ Hz)	Yes
B/Transition	58447–58574	78–205	1.6	$\sim 0.05$	...	Low $\nu$ ( $< 10^{-5}$ Hz)	Yes
C/Hard	58576–58717	207–348	1.2	$\sim 0.03$	PL dominated	Low+high $\nu$ ( $< 10^{-3}$ Hz)	No
D/Hard	58721–58858	352–489	1.2	$\sim 0.03$	PL dominated	Low+high $\nu$ ( $< 10^{-3}$ Hz)	Yes
E/Quiescent	58930–...	561–...	$> 1.9$	$< 0.0004$	...	...	...

**Note.** The phase is referenced with respect to the discovery epoch.  $f_{\text{Edd}}$  is the bolometric Eddington fraction of emission. BB stands for blackbody; PL stands for power law.

time-resolved NICER stacked spectra (0.4–2 keV; doi:10.5281/zenodo.4646229). All analysis is performed using XSPEC version 12.10.0 in HEASOFT v6.24. Best-fit model parameter uncertainties are estimated using the `error` command in XSPEC.

We find no evidence for additional intrinsic absorption in the earliest Swift spectrum, which might be expected if the disk is initially in a slim state (Wen et al. 2020) (recalling that we find a peak mass accretion rate  $\sim$  the Eddington rate). None of the later spectra show evidence for additional neutral absorption either. Therefore, we fix the hydrogen column density to the Galactic foreground value of  $n_{\text{H}} = 1.15 \times 10^{20} \text{ cm}^{-2}$  (HI4PI Collaboration et al. 2016) for all subsequent analysis.

For spectral analysis we only used the EPIC-pn data. We bin the two EPIC/pn spectra to a minimum of 25 counts per spectral bin and oversample by a factor of 3. We first attempt to fit the spectra using a single component: a blackbody model (`bbody`), as well as multicolor blackbody (`diskbb`), power-law (`powerlaw`), and thermally Comptonized continuum models (`Nthcomp`). None of these describe the data well (reduced chi-squared value  $\chi_r > 1.6$ ). Strong systematic residuals are apparent in all cases.

We next employ a thermal model to describe the soft energies ( $< 1.5$  keV) and a power-law model to describe the higher energies (see Figure 5). Fitting a power law to higher energies only, we find a very large soft excess below 1.5 keV for XMM1 (factor  $> 30$  at 0.3 keV), suggesting that relativistic reflection models cannot account for the spectral shape, although we did not explore detailed reflection spectral modeling. We note that the soft excess we refer to is soft X-ray emission in addition to power-law X-ray emission and does not refer to the pure blackbody spectra observed in some TDEs. We next add a thermal component to describe the soft energies. We first try `TBabs`  $\times$  `zashift`  $\times$  (`diskbb` + `powerlaw`) in XSPEC, which yields temperatures  $kT = 123$  and 146 eV for XMM1 and XMM2, respectively. The power-law index  $\Gamma \sim 3.3 \pm 1.0$  is steep at early times (although the errors are large), but at late times it becomes well constrained  $\Gamma = 2.1 \pm 0.1$ . We note that the reduced  $\chi^2$  is marginally statistically acceptable for both fits (reduced chi square of  $\chi_r = 1.29$  and 1.32, respectively; see Table 4). We find significant evolution in the power-law contribution to the total X-ray flux between XMM1 and XMM2, increasing from  $\sim 0.25$  to 0.64. Using a more physically motivated model, `TBabs`  $\times$  `zashift`  $\times$  (`diskbb` + `nthcomp`), where the Comptonizing seed photon temperature is linked to the accretion disk temperature, yields similar results.

Employing instead a bremsstrahlung model (`bremss`) for the thermal component provides better quality of fit. Using this model, we find plasma temperatures of  $kT = 210$  and 290 eV,

while the power-law indices remain constant at  $\Gamma \sim 1.9$ , for  $\chi_r = 1.08$  and 1.07, respectively. In agreement with the `diskbb` model results, we find that the power-law fraction of emission increases from near negligible ( $0.05 \pm 0.03$ ) to providing a dominant ( $0.54 \pm 0.04$ ) contribution to the total X-ray flux.

### 3.4.2. Power-law Fraction of Emission

Time-resolved spectra from NICER over the first  $\sim 450$  days provide further clear evidence for significant spectral evolution. Background-subtracted, unbinned spectra are fit to the same thermal + power-law models employed for the XMM analysis in `xspec`, using Cash statistics (Cash 1979). The fits are conducted in the 0.4–2 keV band, and reported luminosities refer to this energy range. This particular bandpass was chosen to minimize the background contamination (see Section 2.3 for more details). The effects of imperfect background subtraction can become significant when the power-law flux is low. For power-law fluxes  $< 10^{-13} \text{ erg cm}^{-2} \text{ s}^{-1}$ , the power-law index is therefore fixed at the best-fit value of the composite ( $\sim 310$  ks) spectrum to mitigate these effects.

The fractional contribution of the power-law component with respect to the total flux is estimated from each of these fits. The evolution of the power-law fraction of X-ray emission, i.e., the relative strength of the corona, is shown in Figure 6 (left panel) for the `diskbb`+`powerlaw` model. For consistency, we also refit the Swift and XMM-Newton spectra in the 0.4–2 keV energy range; we note that these results are consistent with those obtained from 0.3 to 10 keV spectral fits for Swift and XMM-Newton observations. The spectra at early times (state A and early state B) are dominated by a thermal component, which provides 50%–95% of the X-ray flux (0.3–10 keV), indicating the presence of a weak corona. In the hard states the corona strengthens to provide  $\sim 60\%$ –80% of the X-ray flux. A similar increase in power-law fraction from near negligible ( $< 15\%$ ) in the soft state to very significant (20%–75%) in the hard state is also found for the `bremss` + `powerlaw` model. To remain agnostic about the nature of the soft excess emission, we perform a similar calculation but this time taking the ratio of power-law flux over the bolometric emission (Figure 6, right panel). This yields a qualitatively very similar picture, with an initially weak corona that subsequently strengthens over time. This evolution is further corroborated by the Swift and XMM-Newton data (Figure 7), which shows a steady increase in the fraction of hard X-ray count rate to total X-ray emission.

We conclude that there is significant spectral evolution in AT2018fyk, where the corona is energetically unimportant at early times, while it produces more than half of the observed X-ray flux, and a significant fraction of the bolometric emission, at late times. This evolution is consistent with a

**Table 4**  
Best-fit Parameters Obtained from X-Ray Spectral Modeling of Swift and XMM-Newton Data

Spectrum	Count Rate (counts s <sup>-1</sup> )	State	$t_{\text{exp}}$ (ks)	Model	$kT$ (eV)	norm( $kT$ )	$\Gamma$	log <sub>10</sub> (norm ( $\Gamma$ ))	log <sub>10</sub> (flux) (erg cm <sup>-2</sup> s <sup>-1</sup> )	PL frac	$\chi^2$ (dof)
XRT	0.037	A	37.6	diskbb	142 ± 10	260 ± 150	2.8 <sup>+1.1</sup> <sub>-1.0</sub>	-4.2 ± 0.3	-11.89 ± 0.03	0.25 ± 0.13	1.30 (40)
				bremss	260 ± 25	0.0037 ± 0.0005	1.8 <sup>+1.4</sup> <sub>-1.1</sub>	-4.7 ± 0.5	-11.87 ± 0.03	0.10 <sup>+0.12</sup> <sub>-0.04</sub>	1.24 (40)
EPIC/pn	0.87	B	13.8	diskbb	123 <sup>+8</sup> <sub>-4</sub>	506 <sup>+103</sup> <sub>-238</sub>	3.3 <sup>+1.1</sup> <sub>-1.0</sub>	-4.5 <sup>+0.2</sup> <sub>-0.3</sub>	-11.96 ± 0.02	0.27 <sup>+0.26</sup> <sub>-0.20</sub>	1.29 (26)
				bremss	210 ± 8	0.0050 ± 0.0004	1.8 <sup>+0.8</sup> <sub>-0.7</sub>	-5.0 ± 0.3	-11.94 ± 0.01	0.05 ± 0.03	1.08 (26)
XRT	0.097	B	30.0	diskbb	166 ± 15	160 <sup>+80</sup> <sub>-30</sub>	2.11 ± 0.17	-3.37 ± 0.06	-11.44 ± 0.02	0.63 ± 0.07	0.82 (95)
				bremss	330 ± 50	0.0034 ± 0.0006	2.0 ± 0.2	-3.43 ± 0.03	-11.43 ± 0.02	0.43 <sup>+0.05</sup> <sub>-0.10</sub>	0.86 (95)
XRT	0.13	C + D	110.4	diskbb	179 ± 8	131 ± 25	2.19 ± 0.08	-3.19 ± 0.05	-11.31 ± 0.01	0.68 ± 0.04	0.92 (214)
				bremss	372 ± 26	0.0036 ± 0.0003	2.06 ± 0.11	-3.27 ± 0.05	-11.31 ± 0.01	0.59 ± 0.05	0.98 (214)
EPIC/pn	1.13	D	24.6	diskbb	146 ± 7	171 <sup>+40</sup> <sub>-30</sub>	2.10 ± 0.08	-3.60 ± 0.03	-11.69 ± 0.01	0.64 ± 0.03	1.32 (90)
				bremss	292 ± 19	0.0024 ± 0.0002	1.93 ± 0.09	-3.69 ± 0.05	-11.67 ± 0.02	0.54 ± 0.04	1.07 (90)

**Note.** The states are as labeled in Figure 4; states C and D are spectrally identical, and only one Swift stacked spectrum is produced covering both. The mean count rate for each spectrum is given in the second column. The effective exposure time  $t_{\text{exp}}$  is given in kiloseconds. The spectral model used is TBabs × zashift × (model + powerlaw), where the model is listed in the table;  $kT$  is the temperature of the thermal component, while  $\Gamma$  denotes the power-law spectral index. Normalizations for the thermal and power-law components are listed in the norm( $kT$ ) and norm( $\Gamma$ ) columns. The flux is integrated from 0.3 to 10 keV. PL frac denotes the fractional contribution of the power-law component to the total X-ray flux. The final column lists the reduced  $\chi^2$  and degrees of freedom (dof).

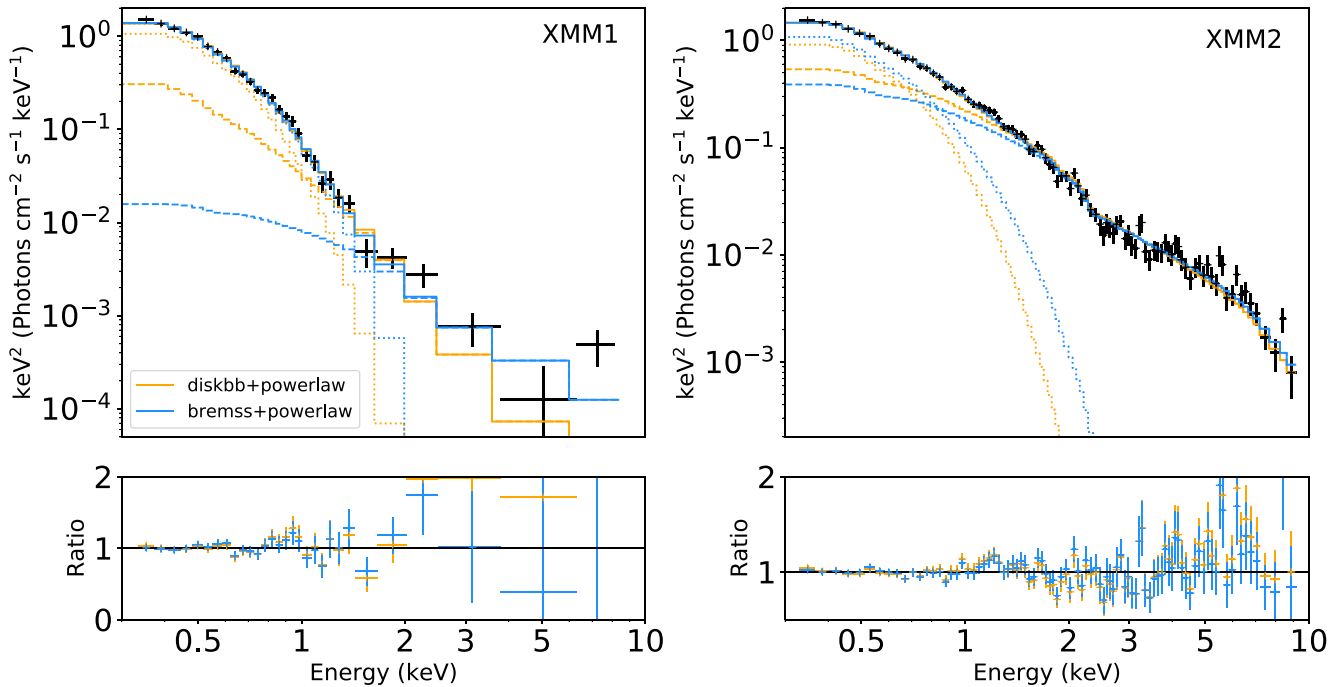


**Figure 5.** XMM-Newton EPIC/pn X-ray spectra (black), overlaid by two best-fit models (diskbb+powerlaw in orange, bremsstrahlung+powerlaw in blue). Dashed lines represent the power-law model, while dotted lines show the thermal component, and solid lines are the sum of the two. The bottom panels show the ratio of data and model. The power-law spectral component is stronger in XMM2 than during XMM1.

spectral state transition from a soft state to a hard state, analogous to those seen in XRBs, AGNs (Done & Gierliński 2005; Remillard & McClintock 2006), and a sample of X-ray-bright TDEs (Wevers 2020).

### 3.4.3. Rapid Spectral Variability

In terms of rapid (timescale of  $\sim$ minutes to tens of hours) spectral variability, the hardness ratio of the X-ray emission as observed by Swift and XMM-Newton can vary on short timescales (Figure 7). However, this variability does not obviously correlate with the X-ray flares. We do not have high-quality spectroscopic X-ray data to assess spectral variability on rapid timescales of tens of minutes (e.g., as seen in quasiperiodic eruptions; Miniutti et al. 2019; Giustini et al. 2020). Analysis of Swift spectra stacked based on their X-ray count rate does not reveal significant spectral changes. The XMM-Newton hardness fraction is constant during the soft state (XMM1) with an average value of  $0.016 \pm 0.015$ , i.e., consistent with 0. However, the hardness fraction varies smoothly between 0.07 and 0.22, with an average value of  $0.15 \pm 0.03$  during the hard state (XMM2). Interestingly, roughly 27,000 s after the start of the exposure there is a hardness flare that coincides with a flux enhancement in the light curve (see Figures 4 and 7).

### 3.5. X-Ray Timing Analysis

To constrain the power spectra for the intervals of the light curve identified with the soft (state A) and hard (state C+D) states (including the corresponding XMM-Newton light curves), we fit the power spectra using the power spectral response (PSRESP) method (Uttley et al. 2002). PSRESP compares the observed power spectra with those of simulated light curves for a given power spectral shape, resampled to match the gaps in the sampling of the real light curves, so that

the distorting effects of sampling on the power spectrum are properly accounted for.

For the Swift/XRT light curves we first rebin the light curves to give one flux measurement per observation and remove a small amount of data with signal-to-noise ratio (S/N) < 1. The light curves are then further rebinned into 2-day bins (slightly larger than the average sampling interval of 1.8 days in states C+D and 1.2 days in state A), and gaps are filled by linear interpolation. The XMM-Newton light curves are binned at 200 s resolution, and gaps are also filled by linear interpolation. We calculate the observed power spectra from the resulting light curves, binning the log-power values geometrically in frequency by a factor of 1.5 (with a minimum of two data points per frequency bin).

The Monte Carlo-simulated underlying time series are generated using a sharply bending power-law model, parameterized by low-frequency index  $\alpha_{\text{LF}}$ , high-frequency index  $\alpha_{\text{HF}}$ , and bend frequency  $\nu_{\text{bend}}$ . For the Swift/XRT data the simulation time resolution is set to 5760 s to roughly match the Swift orbital period and ensure that there are 30 simulated data points per 2-day bin. We account for the missing simulated power on timescales from 5670 s down to the duration of each Swift snapshot ( $\sim$ 1 ks) by calculating the rms of the model on those timescales and adding a Gaussian random number with the same standard deviation to each sampled simulated data point. By accounting for random variations, this is an advance over the original PSRESP, which accounted for this effect by adding a constant component to the simulated power spectrum and assuming that the log-power errors scaled with those of the simulation.

To match the observed data, 200 s sampling is used for the XMM-Newton light-curve simulations. In the PSRESP software, the simulations are resampled to match the sampling of the unbinned light curves, and rebinned and interpolated in the

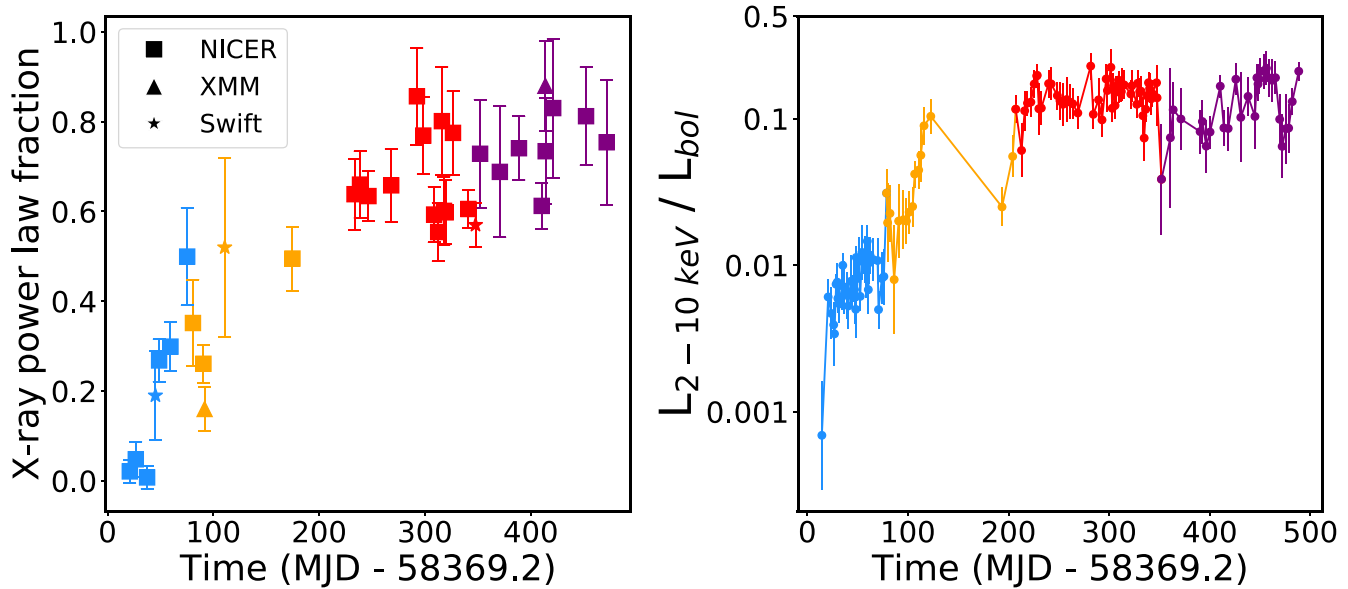


**Figure 6.** Long-term evolution of the X-ray corona. Left: fractional contribution of the power-law component to the total X-ray flux, i.e., a measure of the X-ray corona’s strength, derived from NICER (squares), Swift (stars), and XMM-Newton (triangles) spectral fits in the 0.4–2 keV band. Colors are the same as in Figure 4. The results are consistent with spectral fits in the 0.3–10 keV energy range of Swift and XMM-Newton (right panel and Table 4). Right: fractional contribution of the 2–10 keV power-law emission to the total bolometric luminosity, as derived from Swift measurements. Errors are added in quadrature but exclude the uncertainty in the  $M$ - $\sigma$  relation ( $\sim 0.4$  dex). The corona contribution is negligible at early times but becomes very significant after +200 days, indicating the strengthening of the corona over time. Data to reproduce this figure are available on Zenodo (doi:10.5281/zenodo.4646229).

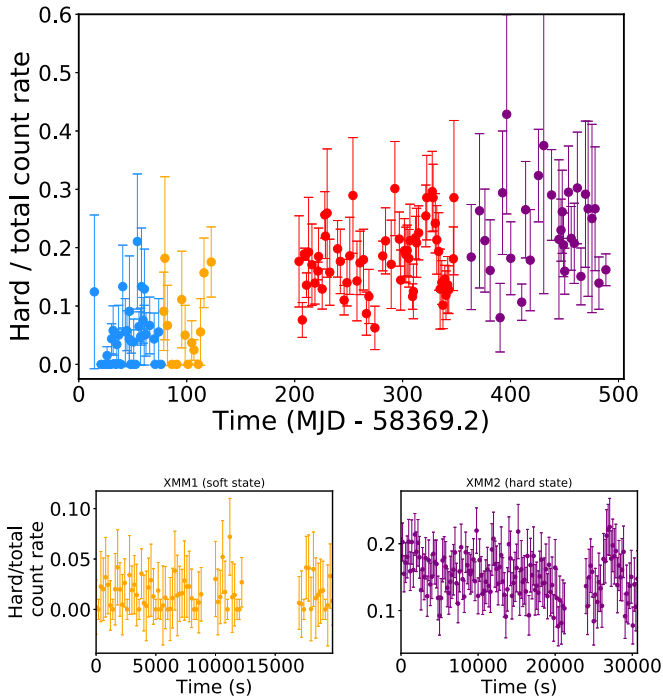


**Figure 7.** Hard-to-total count rate ( $[1.5\text{--}10 \text{ keV}]/[0.3\text{--}10 \text{ keV}]$ ) as a function of time as measured by Swift/XRT (top) and XMM-Newton/EPIC (bottom). The evolution is consistent with results from time-resolved spectra shown in Figure 6, i.e., hard X-rays dominate in states C and D. Data to reproduce this figure are available on Zenodo (doi:10.5281/zenodo.4646229).

same way as the data, so the effects on the power spectrum are accounted for.

For each observed light curve, we generate 1024 simulated light curves as segments cut from a single very long light curve (to account for low-frequency “red-noise leak”; Uttley et al. 2002). Unlike in the original PSRESP, which added observational

(“Poisson”) noise as a constant power spectral component, we include the effects of observational noise by simulating separate noise data sets from Gaussian errors that match the observed errors on each data point, resampling, interpolating, and adding the resulting noise spectrum to the simulated light curve power spectrum. By separating the noise contribution in this way, we can use an arbitrary normalization to fit the simulated intrinsic power spectra to the data, without needing to specify the observed S/N as an additional variable to be stepped through in the parameter search.

As in the original PSRESP, the simulated light curves are used to calculate the mean and standard deviation on the log-power in each frequency bin, and for a given set of model parameters we can compare this with the observed power spectrum to yield a “pseudo”- $\chi^2$  value for the distorted power spectrum,  $\chi_{\text{dist}}^2$ , of a given pair (Swift/XRT and XMM-Newton) of light curves. We minimize  $\chi_{\text{dist}}^2$  to obtain the best-fit normalization for the given shape parameters of the power spectral model (power-law indices and bend frequency). By comparing the  $\chi_{\text{dist}}^2$  of the observed power spectrum with those of the simulations for a given model, we can estimate a goodness of fit for that model.

In the original PSRESP, contours of goodness of fit are used to obtain errors on the power spectral parameters. However, as noted by Marshall (2015), this approach can lead to acceptance regions that are too small when the best-fit goodness of fit is itself low. From the comparison of  $\chi_{\text{dist}}^2$  of the best-fit models with the goodness of fit derived from the simulations, we are able to identify that for this particular set of light-curve samples  $\chi_{\text{dist}}^2$  behaves closely to an undistorted  $\chi^2$  distribution. Therefore, we estimate confidence contours on the model parameters using the standard  $\Delta\chi^2$  approach (which is equivalent to likelihood ratio, for normally distributed errors).

To limit the parameter space covered, we consider two “typical” values of low-frequency slope,  $\alpha_{\text{LF}} = 0$ , corresponding to the low-frequency shape of the “band-limited noise”

seen in black hole XRB hard states, and  $\alpha_{\text{LF}} = -1$ , corresponding to the intermediate-frequency slope of “broadband noise” seen in faint black hole XRB hard states, or the low-frequency slope that is seen in some soft states of black hole XRBs (see, e.g., Heil et al. 2015 for a comparison of the range of XRB power spectral shapes). For each of these two low-frequency slopes, we search a parameter space covering a wide range of bend frequency (searched in equally spaced intervals of  $\log(\text{bend frequency})$ ) and high-frequency slope (searched in equal intervals of the power-law index). We obtain confidence intervals on the power density spectra (PDS) by Monte Carlo likelihood sampling of the fitted model parameters, the bend frequency and the high-frequency slope.

Both low-frequency shapes,  $\alpha_{\text{LF}} = 0$  and  $\alpha_{\text{LF}} = -1$ , provide adequate fits to the hard-state data over some of their parameter space, with best-fit goodness of fits of 0.28 and 0.19, respectively. The confidence contours for the two types of model considered and plots of the best-fit model (distorted and underlying) versus the data are shown in Figure 8. The best-fit parameters, their one-dimensional ( $1\sigma$ ) errors, and fractional rms (integrated from the model over  $10^{-7}$  to  $10^{-3}$  Hz) are provided in Table 5. The high-frequency slopes we measure are similar to those measured for AGN samples, which have slopes of  $\alpha_{\text{HF}} \approx -2$  (if no bend is required for the PDS) to  $-3$  (if the PDS requires a bending power-law; González-Martín & Vaughan 2012). Note that the high-frequency slope is not well constrained for large negative indices owing to red-noise leak effects (Uttley et al. 2002).

Since either model provides a good fit to the hard-state interval, we cannot distinguish the type of hard state solely on the basis of the power spectral shape, but we note that the inferred broadband fractional rms of 55% is much more consistent with black hole XRB hard states than with the soft states (which show rms < a few percent).

#### 4. Discussion

The emission of the outer accretion disk around a  $10^{7.7} M_{\odot}$  black hole peaks in the UV band, which we monitored using the Neil Gehrels Swift satellite. Swift also performed monitoring observations in X-rays (0.3–10 keV), which contain information about the poorly understood components referred to as the soft excess (dominating the 0.3–1.5 keV band) and the X-ray corona (emitting primarily between 2 and 10 keV). The nature of the former component is still unclear, but it could originate in the inner accretion disk either directly (although the observed temperature may be too high for this in AT2018fyk) or from a low-temperature Comptonization component in the inner regions, while the standard corona likely originates in a hot plasma above the inner disk. We also monitored for radio emission to search for signatures of a newly launched jet. These data provide three key diagnostics to characterize the accretion properties following the TDE, which together enable detailed comparison with stellar-mass black holes.

First, the long-term light curves (top left panel of Figure 4) allow us to track the evolution of the SED, using the UV to X-ray spectral slope  $\alpha_{\text{ox}}$  (Section 3.3). This quantity represents the relative strength of the accretion disk (in the UV at 2500 Å) and the corona (at 2 keV) and serves as a proxy for accretion state. In stellar-mass black holes, the strength of the disk relative to the corona changes as a function of the Eddington ratio  $f_{\text{Edd, bol}}$  (Fender et al. 2004; Remillard & McClintock 2006). Appropriate mass scaling of the relative component

strengths, represented by  $\alpha_{\text{ox}}$  in SMBHs, also reproduces the observed properties of large samples of AGNs and relatively fast evolving changing-look AGNs (Sobolewska et al. 2011b; Ruan et al. 2019); we reiterate that there is potentially a significant (systematic) uncertainty in the black hole mass estimate for AT2018fyk, which should be taken into account when making the comparison to (changing-look) AGN behavior. Given that the uncertainty is systematic, the shape of the evolution throughout the diagram will not change as a result.

Second, to characterize the X-ray spectra in the different phases, we use a two-component spectral model (Section 3.4), including a thermal component to describe the soft energies (0.3–2 keV) and a power-law to account for the harder X-rays (2–10 keV). The key diagnostics are the ratio of the power-law spectral component flux to the total emission in X-rays and the ratio of power-law emission to the total bolometric luminosity (including the accretion disk, soft excess, and corona). These quantities are indicators of accretion state, and their evolution is presented in Figure 6.

Third, photometric variability properties of the X-ray emission are analyzed by using the PDS derived from the Swift and XMM-Newton light curves in the different phases (Figure 8; see also Section 3.5). The Swift light curves provide constraints on long timescales (1–25 days), while the XMM-Newton light curves probe short timescales (minutes to hours). In Figure 8 we compare the soft and hard spectral state power spectra. The best-fit model parameters are constrained using Monte Carlo light-curve simulations, which are fit using a bending power-law model (see Section 3.5).

Using these diagnostic tools, we investigate the properties of AT2018fyk in each of the phases defined in Figure 4 and find remarkable similarities to the properties of accreting stellar-mass black holes. The  $\alpha_{\text{ox}}$  evolution with  $f_{\text{Edd, bol}}$  is strikingly similar to predictions from scaling a stellar-mass black hole outburst (Sobolewska et al. 2011b; Figure 3 of Ruan et al. 2019); we show a direct comparison with XRB outburst evolution across the hardness–intensity diagram (HID) in Figure 9, which further illustrates the similarities between these systems.

##### 4.1. Soft-to-hard Accretion State Transition

At the time of discovery, we find AT2018fyk at high  $\alpha_{\text{ox}}$ , with an X-ray spectrum dominated by thermal emission with a temperature of  $kT = 120\text{--}140$  eV. The bolometric luminosity peaks around  $L_{\text{bol}} \approx 0.1L_{\text{Edd}}$  and is already declining, suggesting that we missed the rise to peak. The corona is present but weak, contributing only 5%–25% of the X-ray flux and a few percent of the bolometric luminosity. This is consistent with the power-law fraction observed in outbursting stellar-mass black holes in the soft state ( $\sim 1\%\text{--}60\%$ ; e.g., Dunn et al. 2010), but inconsistent with the properties of soft-state AGNs, where the corona is typically dominant (e.g., even for highly accreting narrow-line Seyfert 1 AGNs the PL fraction is on average 70%, see, e.g., Vaughan et al. 1999; Gliozzi & Williams 2020; see also Section 4.7 for a more elaborate comparison to AGNs). The source is not detected at radio wavelengths (radio luminosity/X-ray luminosity =  $L_{\text{radio}}/L_{\text{X}} \lesssim 10^{-6}$ , Wevers et al. 2019a), and we find no significant photometric variability on short timescales (frequencies  $\gtrsim 10^{-6}$  Hz; see Figure 8). These properties are analogous to the soft states of stellar-mass

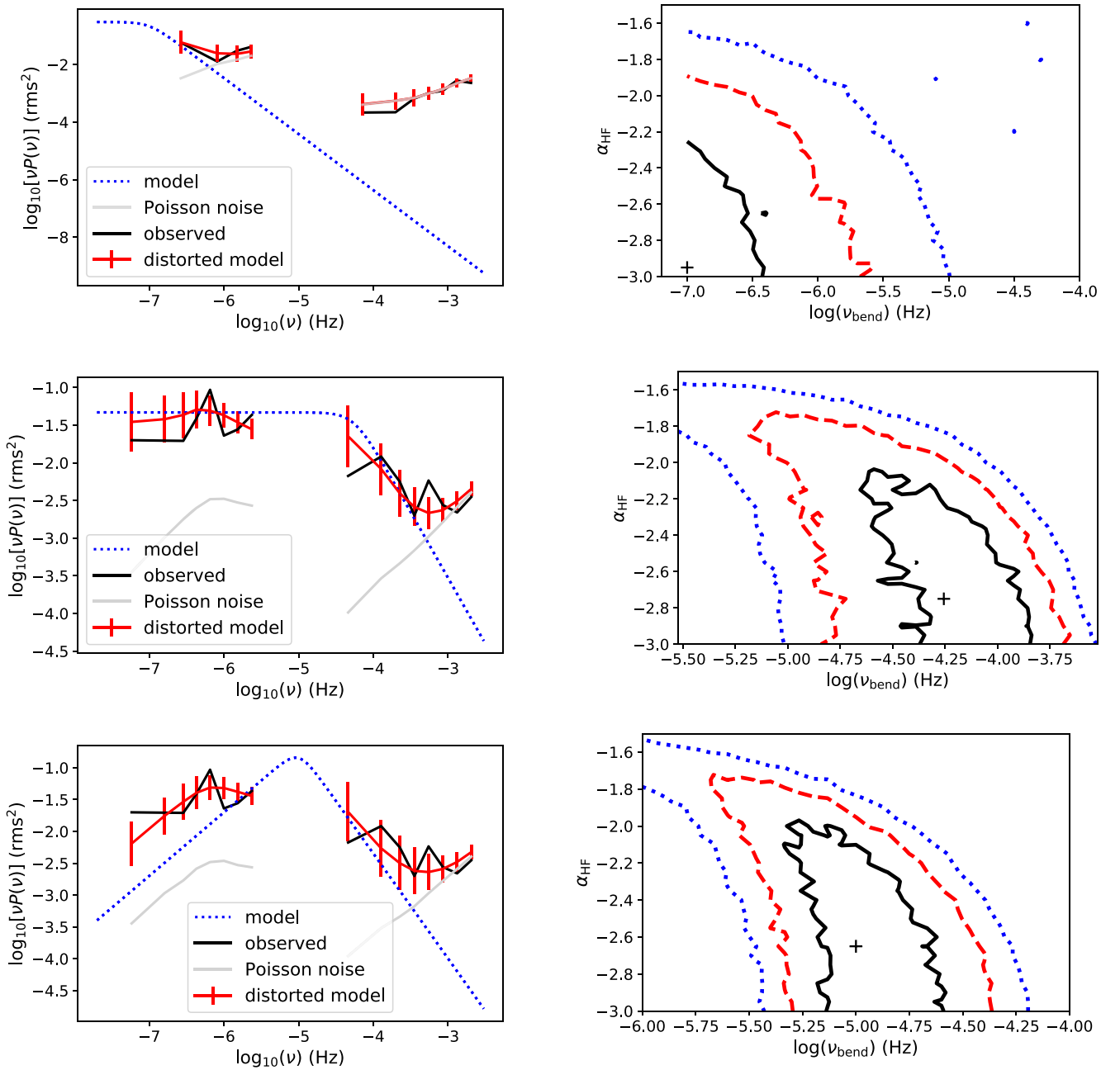


**Figure 8.** Power spectra and confidence contours in the soft (top panels) and hard states (middle/bottom panels). Left: power density spectra. Observations are shown as solid black lines, the best-fit distorted model is shown in red, the undistorted model is shown in blue, and Poisson noise levels are indicated in gray. The soft state is shown in the top panels; no bend in the power-law model is required to reproduce the data. For high frequencies ( $\gtrsim 10^{-6}$  Hz) the data (black) are consistent with Poisson noise (gray curve). The middle and bottom panels show the hard state, with the low-frequency slope fixed to  $\alpha_{LF} = -1$  and  $\alpha_{LF} = 0$ , respectively. Variability on frequencies between  $10^{-7}$  and  $10^{-3}$  Hz is evident; a bend is required to reproduce the data. Right panels: corresponding confidence contours between the bend frequency and the high-frequency slope of the power spectrum for  $1\sigma$ ,  $2\sigma$ , and  $3\sigma$  confidence regions (solid black, red dashed, and blue dotted lines, respectively), corresponding to  $\delta\chi^2 \simeq 2.3$ , 6.18, and 11.83 respectively. Black plus signs mark the best-fit set of parameters.

black holes (Homan & Belloni 2005; Remillard & McClintock 2006).

When  $f_{\text{Edd,bol}}$  drops below  $\sim 0.05$ , roughly consistent with the typical transition luminosities of stellar-mass black holes (ranging from a few to  $\sim 10\%$ ; Maccarone et al. 2003), AT2018fyk transitions into an intermediate state (phase B). Both the SED (i.e.,  $\alpha_{\text{ox}}$ ; top right panel of Figure 4) and the X-ray spectrum harden significantly over time (Figure 6). The observations show an increase in the X-ray power-law fraction (hardening), as well as an increasingly significant contribution of the power law to the total bolometric luminosity. This is

consistent with a scenario where the inner accretion disk becomes very cool or evaporates and the relative strength of the corona increases.

When the source reaches phase C,  $\alpha_{\text{ox}}$  stabilizes, the power-law component dominates the X-ray spectrum (providing  $>50\%$  of the X-ray flux), and the X-ray flux varies dramatically. Rapid, large-amplitude variability is present on both short (a few tens of minutes; bottom right panel of Figure 4) and long (days; top left panel of Figure 4) timescales. The onset of fast variability on roughly 10-minute timescales is indicative of emission dominated by a compact emitting region,

**Table 5**  
Results of the Power Spectral Fitting

State	$\log(\nu_{\text{bend}})$ (Hz)	$\alpha_{\text{HF}}$ ( $10^{-7}$ to $10^{-3}$ Hz)	rms (%) ( $10^{-7}$ to $10^{-6}$ Hz)	rms (%) ( $10^{-6}$ to $10^{-5}$ Hz)	rms (%) ( $10^{-5}$ to $10^{-3}$ Hz)	rms (%) ( $M_{\odot}$ )	$\log(M_{\text{BH}})$
Hard ( $\alpha_{\text{LF}} = 0$ )	$-5.00^{+0.33}_{-0.27}$	$-2.65 + 0.5^*$	$54 \pm 1$	$13^{+4}_{-3}$	$39^{+5}_{-8}$	$35^{+7}_{-8}$	$7.25 \pm 0.55$
Hard ( $\alpha_{\text{LF}} = -1$ )	$-4.26^{+0.33}_{-0.20}$	$-2.75 + 0.5^*$	$55^{+1}_{-3}$	$32^{+4}_{-3}$	$32^{+5}_{-8}$	$31^{+7}_{-8}$	$6.9 \pm 0.55$
Soft	$< -5.5^a$	$-2.95 + 0.5^*$	$21^b$	$32^{+4}_{-7}$	$7^{+2}_{-1}$	$1^{+1}_{-0.5}$	...

**Notes.** The rms values are reported in various frequency bands. The black hole mass is calculated using the bend frequency in combination with the relation of McHardy et al. (2006). Values marked with an asterisk have negative error bars bounded by the parameter range.

<sup>a</sup> 99% confidence upper limit.

<sup>b</sup> 99% confidence lower limit (the upper range of rms is not well constrained since the low-frequency power spectral shape is not well constrained by the soft-state light curve).

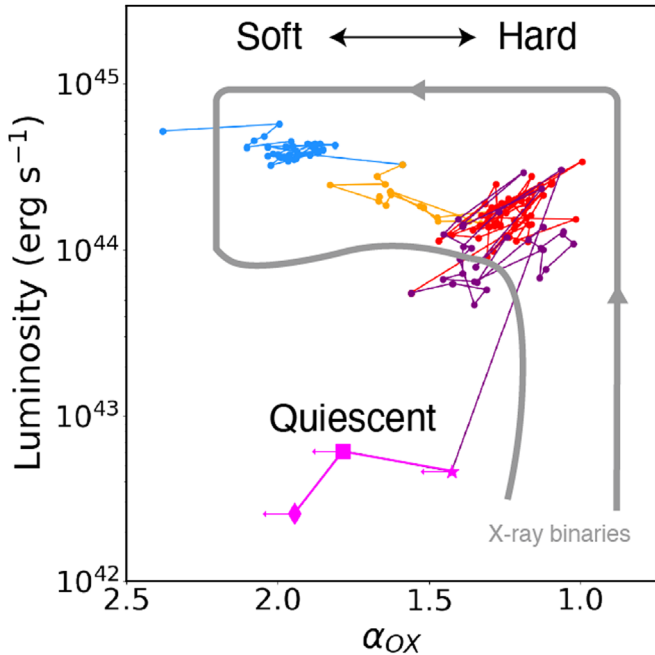


**Figure 9.** AT2018fyk in the hardness–intensity diagram; hardness is represented by  $\alpha_{\text{ox}}$ . Note that we have reversed the horizontal axis to reproduce the classical HID. The gray bands show the typical turtle-head evolution of stellar-mass black holes in outburst. The TDE was discovered after peak light in the soft state; the observations missed the equivalent of the rising phase and hard-to-soft transition in XRBs (segments marked with gray arrows).

namely, an X-ray corona (see Sections 3.5 and 4.2). We note that the power-law contribution to the bolometric output in this state is similar to that seen in type 1 AGNs with Eddington ratios  $\sim 0.01$  (Lusso et al. 2010; see also Figure 11).

The ratio of radio to X-ray luminosity is constrained to  $\lesssim 4.5 \times 10^{-7}$  in AT2018fyk. This rules out the appearance of a powerful radio jet, which is generally present in XRB hard states. Except for the absence of a radio jet, discussed in more detail in Section 4.3, the rest of the properties are consistent with typical hard states found in XRBs and AGNs (Homan & Belloni 2005; Körding et al. 2006b; Remillard & McClintock 2006). While the spectral hardening can, in principle, be due to variable absorption columns, the contemporaneous change in  $\alpha_{\text{ox}}$ , as well as the change in timing properties, cannot be explained in this way. Instead, this indicates that the disk transitioned from a thermal-dominated soft state to a radiatively inefficient, power-law/non-thermal-dominated hard state.

X-ray flaring follows the soft-to-hard transition, when the thermal X-ray component has decreased in flux by  $\sim 50\%$ , while the power law brightens by more than an order of magnitude. Rapid flares occur only in the X-ray band, indicating that they are confined to the hot, inner part of the accretion flow. While the X-ray spectral and photometric behavior remains unchanged in the hard states (state C+D), the UV light curve in phase C is roughly constant, whereas in phase D there are significant brightness variations (Figure 4, top left panel). The final phase (state D) of the UV light curve is remarkable, showing two cycles of *modulations* on  $\sim 50$ -day timescales. There is no significant correlation between the UV and X-ray variability, which suggests physically distinct regions for these two phenomena.

#### 4.2. Changes in the Timing Properties: Appearance of a Band-limited High-frequency Component

The soft-state power spectrum (Figure 8) is very different from that seen in the hard state, as unlike the hard-state power spectrum, it can be well fitted (goodness of fit = 0.7) with a single steep power law at low frequencies, with no power spectral break to flatter slope required. The parameter confidence contours were obtained by assuming a low-frequency slope of  $\alpha_{\text{LF}} = -1$  to have the best chance of matching the low-frequency variability seen in the light curve, but a steeper slope extending to low frequencies is still preferred.

The soft state shows a smaller fractional rms than the hard state, but this is concentrated entirely at low frequencies ( $< 10^{-6}$  Hz), while in the hard state a significant fraction of variability occurs above  $10^{-5}$  Hz, as is apparent from the much more variable XMM-Newton light curve.

In Figure 8 we compare the soft- and hard-state power spectra directly. The lower bend frequency in the  $\alpha_{\text{LF}} = 0$  case makes it a closer match to the low-frequency constraint on the soft-state bend and a more conservative comparison with the soft-state power spectrum. However, the overall shapes of the distorted power spectra should not depend too strongly on the low-frequency index, since both fit the data well.

It is interesting to note that the low-frequency power spectra for both soft and hard states are relatively consistent in amplitude, with a strong divergence in power at higher frequencies. Therefore, we can speculate that the main difference between the soft- and hard-state light curves is the addition of a band-limited high-frequency component during the hard state. An additional broad high-frequency component associated with the harder state is reminiscent of the transition between soft and hard states in XRBs, where band-limited

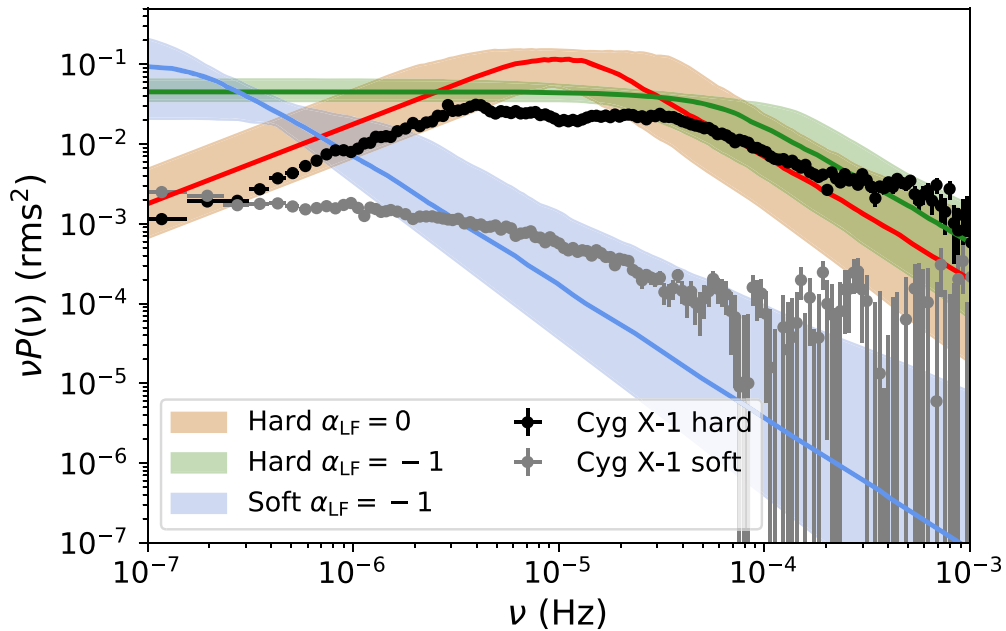


**Figure 10.** Power density spectral models of the soft (state A) and hard (state C+D) states. The median (solid curve) and 95% confidence intervals (shaded regions) of the models are shown. The confidence interval includes the effects of the uncertainty in high-frequency slope and bend frequency. Sampling effects significantly distort the PDS from the Swift data, so we assume two different low-frequency slopes (0 and  $-1$ ) covering the range seen in AGNs and XRBs. Most of the variability/power comes from low frequencies in the soft state, while a high-frequency component ( $\gtrsim 10^{-5}$  Hz) appears in the hard state and dominates the overall variability (see Table 5). This supports the idea that a compact corona dominates emission in the hard state. The black and gray data points show the PDS of a well-observed XRB, Cyg X-1, scaled up to a  $10^7 M_{\text{BH}}$  black hole (see text).

noise at higher frequencies is one of the first components associated with hard-intermediate states immediately prior to or after a transition to/from the soft state (see, e.g., the power spectral evolution presented in Heil et al. 2015).

We measure the break frequency of the red-noise PDS in the hard state and find  $\log(\nu_{\text{bend}}) \approx -4.5$ . This is on the lower end of the distribution of typical break frequencies found in AGNs, which typically occur around  $\nu_{\text{bend}} \sim$  a few  $\times 10^{-4}$  Hz (although a lower-frequency break similar to AT2018fyk has also been observed; González-Martín & Vaughan 2012). Assuming that we can use the break frequency–black hole mass scaling relation derived for AGNs (McHardy et al. 2006) here, we derive a black hole mass of  $\log(M_{\text{BH}}) = (6.9-7.2) \pm 0.55 M_{\odot}$ . This is in agreement to within the uncertainties with the estimate from the  $M$ – $\sigma$  relation (Wevers 2020).

It is evident from the XMM2 light curve (Figure 4, bottom right panel) that the brightness sometimes changes by  $\sim 50\%$  on timescales as short as 1250 s. Using light-travel time arguments, this corresponds to a very compact emission region of  $< 5 R_g$  for the observed X-ray variability, assuming  $M_{\text{BH}} = 10^{7.7 \pm 0.4} M_{\odot}$  (with an upper limit of  $R < 13 R_g$ , allowing for the uncertainty in the  $M_{\text{BH}}$  measurement). These results support a scenario where the fastest X-ray variability originates in a very compact X-ray corona.

For comparison with XRB PDS, we used NICER observations of Cyg X-1 in a hard (ObsID 2636010101) and soft state (ObsID 1100320122), obtaining PDS in, respectively, the 2–10 keV band (representing the hard power-law component variability) and the 0.6–1 keV band (representing the disk blackbody component variability). Although Cyg X-1 shows uncharacteristically high variability amplitude in its soft state compared to other black hole XRBs ( $\sim 10\%$  rms vs.  $< 1\%$  rms; e.g., Heil et al. 2015), the fact that it accretes from a stellar wind (and hence has a relatively small accretion disk) may

make it a better comparison with AGNs, and with TDEs in particular.

PDS characteristic timescales scale inversely with black hole mass and linearly with accretion rate. Assuming the  $\sim 10^7 M_{\odot}$  black hole mass we infer from the measured break timescale of the hard-state TDE power spectrum and a black hole mass of  $\approx 20 M_{\odot}$  for Cyg X-1 (Miller-Jones et al. 2021), combined with the larger (factor 5) accretion rate of the TDE hard state compared to Cyg X-1, we scale the Cyg X-1 PDS by a factor  $10^{-5}$  in frequency for a better comparison with the soft and hard TDE PDS in Figure 10. This figure illustrates the similarity between the XRB and TDE PDS in the soft and hard states.

#### 4.3. Constraints on the Presence of a Jet

TDEs are, in principle, excellent opportunities to study jet formation, as the newly formed accretion flow settles into a steady state. Follow-up campaigns at radio wavelengths are indeed revealing a growing population of radio-bright TDEs (Alexander et al. 2020). It is interesting to note that several (though not all) radio-bright TDEs launch their nonrelativistic jets/outflows already at early times, while they are in the soft state (van Velzen et al. 2016a; Stein et al. 2021). This is at odds with the standard paradigm in XRBs, where the jet is quenched during disk-dominated accretion states (Corbel & Fender 2002; Russell et al. 2011) and the transition of the accretion flow from the soft into the hard state is generally accompanied by the emergence of a compact radio jet (Fender et al. 2003).

While our early observations of AT2018fyk are consistent with quenched jets, if the analogy holds, we would expect the emergence of a radio counterpart following the soft-to-hard-state transition. However, our radio observations, covering the soft, hard, and quiescent states, indicate that no bright radio jet is launched. Using the mean X-ray luminosity ( $3 \times 10^{43}$  erg

$s^{-1}$ ) in the hard state, the fundamental plane (Körding et al. 2006a) predicts a radio luminosity of  $\sim \text{few} \times 10^{39} \text{ erg s}^{-1}$ . Our radio nondetections constrain the luminosity to at least two orders of magnitude lower. We do note that a black hole mass that is lower by about 1 dex ( $\sim 10^{6.7} M_{\odot}$ ) would bring the radio upper limits in line with the scatter observed in the fundamental plane.

While the presence of a correlation among radio luminosity, X-ray luminosity, and black hole mass is well established for black holes accreting in a radiatively inefficient state (Merloni et al. 2003; Falcke et al. 2004), the situation for systems in the process of changing accretion state is less clear. We briefly speculate on which factors might be important to explain the apparent discrepancy with the XRB paradigm.

The emergence of a compact radio jet following the soft-to-hard-state transition has been well documented in XRBs (Fender 2001), although there is a delay of one to several weeks between the transition in the X-ray spectrum and the onset of a radio source (Kalemci et al. 2013; Vahdat Motlagh et al. 2019). The cause of this delay is currently unclear, as is any potential scaling with black hole mass, because multiple conditions need to be satisfied to successfully launch a jet. Kalemci et al. (2013) found that for compact jets to be produced in XRBs, the disk luminosity Eddington fraction needs to be below  $10^{-4}$ . This condition is not fulfilled for AT2018fyk, where the bolometric disk emission Eddington ratio is  $> 10^{-3}$ ; other factors may also play a role. Once a strong corona forms, magnetic fields need to be generated and transported, which is one plausible explanation for the delay seen in XRBs. Alternatively, the corona has to be large enough to efficiently collimate the outflow into a compact radio jet.

If launching a jet requires a significant magnetic field, this will take time to grow via the magnetorotational instability. In contrast to AT2018fyk, several TDEs in the soft state do launch powerful outflows (van Velzen et al. 2016a; Alexander et al. 2020), suggesting that the jet launching mechanism may be driven by other factors (Pasham & van Velzen 2018), such as the availability of magnetic flux. Since the disrupted star is not expected to carry significant magnetic flux, the buildup through dynamos or magnetorotational instabilities may be too slow for most TDEs, unless a fossil magnetic flux reservoir is present (Kelley et al. 2014). We note that the host galaxy spectra of several radio-bright TDEs show possible evidence for nuclear activity. The narrow emission lines, when plotted in a diagnostic emission line diagram, fall in the regions indicative of a low-ionization nuclear emission-line region (LINER), AGN, or composite AGN/star formation (Nikołajuk and Walter 2013; French et al. 2017). While LINER-like emission can also be excited by other emission mechanisms, if instead this indicates recent or ongoing low-level AGN activity, the preexisting jet cone and/or relic magnetic fields may facilitate the renewed launching of an outflow. AT2018fyk, on the other hand, does not show indications of recent AGN or star-forming activity, so the absence of relic magnetic fields may also help explain the lack of a radio jet.

#### 4.4. Hard-state-to-quiescence Transition

The strong UV and X-ray variability ends with a transition into a different regime (the quiescent state, E), evidenced by a factor of  $\sim 15$  drop in the UV luminosity and a factor of  $> 5000$  in X-rays. As a result, the SED significantly softens, i.e.,  $\alpha_{\text{ox}}$

increases, and the UV emission becomes relatively more important when compared to the hard state.

These dramatic changes constitute the *second* accretion state transition. Analogous, although much less dramatic, behavior is also seen in stellar-mass black holes, which move toward a baseline, quiescent state at very low accretion rates. For stellar-mass black holes this state is defined empirically by  $L_{\text{X}} < 10^{-5} L_{\text{Edd}}$  (Plotkin et al. 2013), when the anticorrelation between the photon index of the X-ray spectrum and  $L_{\text{X}}$  plateaus or inverts (Homan et al. 2013; Yang et al. 2015). Qualitatively similar behavior is also observed in (changing-look) AGNs (Yang et al. 2015; Ruan et al. 2019).

The transition toward quiescence in stellar-mass black holes and AGNs is more gradual and much less dramatic than observed for AT2018fyk. This warrants a discussion of alternative scenarios (see Section 4.5). For now, we note an important difference between XRBs and AGNs, versus TDEs: the fallback rate of material at the outer disk edge. In stellar-mass black holes and AGNs there is a steady supply of material, whereas in TDEs the supply is expected to decrease rapidly with time (following a  $t^{-5/3}$  power-law behavior; Rees 1988). This may trigger much more dramatic changes in the structural properties of the accretion flow in TDEs. We constrain  $L_{\text{X}} < 2.6 \times 10^{-6} L_{\text{Edd}}$  for AT2018fyk, indicating that the accretion flow has indeed reached the quiescent state and the mass supply rate from the stellar debris has dropped to very low levels.

The increase in  $\alpha_{\text{ox}}$  (softening of emission) at low Eddington ratio has also been observed in stellar-mass black hole outbursts (Homan et al. 2013; Plotkin et al. 2017), as well as in a sample of changing-look AGNs (Ruan et al. 2019). Such a softening cannot be explained by the progressive disk truncation/evaporation thought to be responsible for the hardening of  $\alpha_{\text{ox}}$  from the soft to the hard state (Sobolewska et al. 2011a). Instead, it suggests that the X-ray component is dominated by an entirely different emission mechanism, although observations are sparse and this state is poorly understood (Plotkin et al. 2015). Remarkably, the  $\alpha_{\text{ox}}$  value in the quiescent state (state E) is at least as high as that observed in the soft state (state A), indicating that the X-ray corona is extremely weak or possibly nonexistent.

#### 4.5. Alternative Explanation for the Second State Transition

Several peculiar features in the hard state (specifically, state D), including those discussed above, warrant a closer look at potential alternatives for the standard accretion state transition scenario for the total collapse of the system. Thermal and viscous instabilities are an inherent property of 1D accretion disk theory at sub-Eddington accretion rates (Lightman & Eardley 1974; Shakura & Sunyaev 1976). In particular, Shen & Matzner (2014) predict that a thermal instability occurs when the fallback rate drops below the advection-dominated regime. When this happens, the disk rapidly transitions into a gas-pressure-dominated, radiatively cooled state. Furthermore, in the presence of a sufficiently high rate of material falling back onto the outer disk, they predict limit cycle oscillations between this gas-pressure-dominated state and the initial radiation-pressure-dominated state. More specifically, changes to both the disk radius and thermal state in the presence of fallback are expected, where the addition of low angular momentum material leads to a shrinking of the disk radius. This

increases the disk surface density and can cause the disk to jump back to the advective state for brief periods of time.

The observed behavior in AT2018fyk shows some similarities to theoretical predictions by Shen & Matzner (2014). First, the predicted timescale for the instabilities to manifest is  $\sim 1$  yr, as observed. Second, the blackbody radius inferred in Figure 2 shows an overall decreasing trend over time, as expected. Some oscillations are observed after  $\sim 300$  days, marking the onset of the UV photometric variability. Shen & Matzner (2014) predict that the thermal cycles will end when the mass fallback rate drops below a critical threshold, which typically occurs after a few (two to three) cycles. AT2018fyk goes through two oscillatory cycles with a typical timescale of  $\sim 50$  days before the UV component (the accretion disk) eventually decreases by a large factor. This scenario provides a self-consistent explanation of the long-term behavior, the UV variability, the blackbody radius evolution, the subsequent state transition, and the absence of a radio jet, providing tantalizing evidence that thermal instabilities might occur in nature.

#### 4.6. The Unusually Rapid Evolution of the Accretion Flow

AT2018fyk is only the fourth UV/optical discovered TDE that is persistently X-ray bright for  $\sim 500$  days, the others being ASASSN–14li (Holoien et al. 2016), ASASSN–15oi (Gezari et al. 2017a), and AT2019azh (Hinkle et al. 2021). It shows evidence for a much more rapid disk formation and subsequent evolution when compared to typical TDEs, including the early emergence of Fe II emission lines (Wevers et al. 2019a) and a pronounced second maximum early in the light curve (Dong et al. 2016; Leloudas et al. 2016). The sudden drop in UV luminosity also occurs relatively early when compared to other TDEs, with van Velzen et al. (2019) finding only one TDE (SDSS TDE1) that may have experienced a similar drop in UV brightness 5–10 yr after disruption. Similarly, the sharp decrease of the X-ray emission occurs much more rapidly after disruption than observed in other TDEs (Jonker et al. 2020).

These seemingly peculiar properties suggest that the post-disruption evolution proceeds more rapidly than in the bulk of the TDE population. Such a rapid evolution is expected if the debris streams can violently self-collide upon their return to pericenter, efficiently removing orbital angular momentum and energy. It is, however, unclear (both theoretically and observationally) whether this circularization phase can indeed happen efficiently in the majority of TDEs (Ulmer 1999; Shiokawa et al. 2015; van Velzen et al. 2019).

The dominant mechanism to achieve strong shocks between streams is relativistic apsidal precession, which becomes increasingly important as the black hole mass increases, or alternatively when the star penetrates deeply into the SMBH potential well (high  $\beta = R_p/R_t$ ). Both AT2018fyk and SDSS TDE1 have comparatively high inferred black hole masses in excess of  $10^7 M_\odot$  (Wevers et al. 2017; Wevers 2020) and are UV faint at late times. At the inferred black hole mass of  $(1\text{--}5) \times 10^7 M_\odot$ , relativistic effects are important for all stellar encounters (Stone et al. 2019), providing a natural explanation for the rapid formation and evolution of the accretion flow, which shines brightly in soft X-rays and at UV wavelengths. The rapid subsequent evolution is a natural consequence of a high black hole mass. The Eddington limit in AT2018fyk is  $\sim 10\text{--}50$  times higher than in other well-observed TDEs, which typically have correspondingly lower black hole masses

(Wevers et al. 2017, 2019b; Mockler et al. 2019). These results indicate that black hole mass could be an important factor setting the timescales of the post-disruption debris evolution.

An alternative explanation for rapid evolution could be a particularly low reservoir of debris to accrete from, i.e., a comparatively low mass star. As a result, the system will run out of material more quickly. However, stars with a mass  $\lesssim 0.4 M_\odot$  would be swallowed whole by a nonrotating SMBH in AT2018fyk (e.g., Stone et al. 2019), while a dimensionless spin of  $a > 0.7$  is required to produce an observable disruption for a  $0.1 M_\odot$  star (e.g., Leloudas et al. 2016). Therefore, given the large mass of the black hole in AT2018fyk, it is unlikely that the disrupted stellar mass is significantly smaller when compared to typical TDEs (Mockler et al. 2019; van Velzen et al. 2019; Wen et al. 2020).

A conservative lower limit for the accreted stellar mass can be obtained by making an assumption for the conversion of accretion power to radiation. We calculate the bolometric energy output by piecewise integration of the entire light curve to find a total radiated energy of  $E_{\text{rad}} = (9.4 \pm 0.2) \times 10^{51}$  erg. Assuming a standard radiative efficiency of  $\eta = 0.1$  and taking into account that only half of the stellar debris is available for accretion, the corresponding stellar mass is  $M_\star \approx 0.1 M_\odot$ . We consider this calculation a lower limit to the true stellar mass. First, the assumption of radiatively efficient accretion throughout the TDE’s evolution may not be valid when the source transitions into the hard state, where we may have  $\eta \ll 0.1$ . This could lead to an increase in the estimate of  $M_\star$  by a factor of 2–3, accounting for the observed duration of the soft and hard states, respectively. Second, there are no constraints on the potentially large bolometric correction (up to a factor of 10 or more; van Velzen et al. 2016b) owing to dust absorption and reemission on subparsec scales, which is the dominant contributor in the uncertainty for the radiated energy.

#### 4.7. Comparison of the Corona Properties with AGNs

It is still unclear whether the soft excess spectral component that is ubiquitously observed in AGNs and TDEs is produced at the inner edge of the compact accretion disk, as an additional low-temperature Comptonization component, or elsewhere. This complicates the analogy and interpretation of the power-law fraction of emission as a proxy for accretion state, as is done for XRBs. To mitigate this uncertainty, an alternative approach that is directly analogous to the one employed for stellar-mass black hole systems is to not only consider the X-ray emission but also include the UV emission where the accretion disk is expected to dominate for SMBHs. In Figure 6 (right panel) we show the ratio of the 2–10 keV power-law emission to the total, bolometrically corrected (optical+UV+X-ray) emission (see Section 3.3 for more details on how this correction is applied). We illustrate how AT2018fyk compares to AGN samples in Figure 11. The values in the hard state, at low Eddington ratios ( $\sim 10^{-2}$ ), cover a very similar parameter space to type 1 AGNs (gray triangles; Lusso et al. 2010) and other AGN samples including many NLS1 sources (black stars; Vasudevan & Fabian 2007). However, in the soft state the power-law emission in AT2018fyk is on the low side compared to AGNs with similar Eddington ratios. This could be resolved by taking into account the uncertainties on our black hole mass estimate of  $\sim 0.5$  dex, and it may indicate that the lower end of the mass range is favored. Alternatively, we do not include the

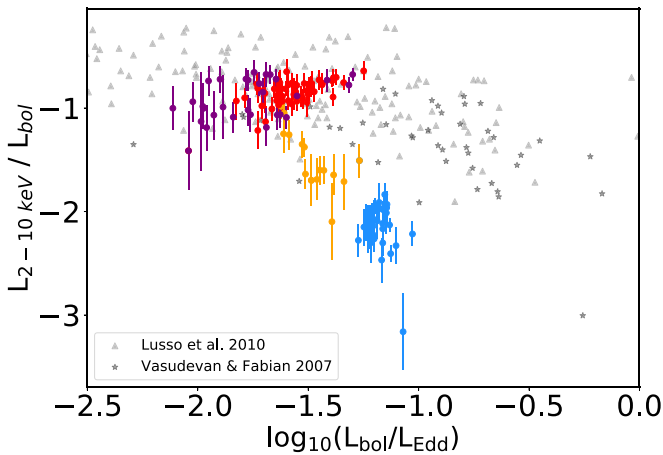


**Figure 11.** Comparison of the evolution of the corona with AGNs. Color-coded filled circles show the evolution of the power-law fraction to the bolometric emission as a function of the Eddington ratio. Gray and black triangles and stars represent AGN samples. Data to reproduce this figure are available on Zenodo (doi:[10.5281/zenodo.4646229](https://doi.org/10.5281/zenodo.4646229)).

full energy ranges used to compute the bolometric corrections in the comparison samples of Lusso et al. (2010) and Vasudevan & Fabian (2007); in particular, we do not have observational constraints for the 10–200 keV band. However, given the steep power-law indices we find, this should result in only small corrections, suggesting that the difference is physical in nature.

We recall that the power-law fraction in the soft state of AT2018fyk is comparable to the values seen in stellar-mass black holes but much lower than in soft-state AGNs. The size of the accretion flow in TDEs (normalized to the black hole gravitational radius) is much more compact than in AGNs. As a result, irradiation and/or radiation pressure are much higher in TDEs (a situation much more like XRBs than in AGNs), which may prevent the formation of an efficient corona shortly after disruption, when the mass accretion rates are highest. Typical soft-state AGNs have been actively accreting material for long periods of time, and hence the corona has had time to build up and stabilize, whereas in the newly formed accretion flow following AT2018fyk we witnessed the formation of the corona in near real time, strengthening as the source moves into the hard state. In the future, a larger TDE sample will help us better understand the formation of the corona and the nature (and role) of the poorly understood soft excess emission component seen in both TDEs and AGNs.

## 5. Summary

We have presented a very rich, multiwavelength set of observations of the TDE AT2018fyk, from peak light (at an Eddington ratio of  $\sim 0.1$ ) into quiescence (Eddington ratio  $< 10^{-3.4}$ ).

We find that around peak light the source exhibits several of the hallmark features of highly accreting SMBHs and stellar-mass black holes in the soft state, including a thermal-dominated X-ray spectrum, a soft (high  $\alpha_{\text{ox}}$ ) SED, no bright radio emission, and exclusively low-frequency ( $< 10^{-5}$  Hz) X-ray variability. After a transition phase, dramatic changes to these properties are observed. The power-law component becomes dominant in the X-ray spectrum,  $\alpha_{\text{ox}}$  hardens significantly, and a band-limited high-frequency ( $\sim 10^{-3}$  Hz) time-variable component appears in the X-ray band. These

changes are consistent with an accretion state transition from a soft to a hard state and a strengthening of the X-ray corona. No bright radio jet accompanies this transition, marking an apparent deviation of the stellar-mass black hole accretion state paradigm. We discuss several plausible explanations for the absence of a radio jet around TDEs and conclude that TDEs showing accretion state transitions provide a promising avenue to better understand the necessary conditions for successful jet formation around SMBHs with future observations.

At late times, a second dramatic transition occurs, with the X-ray luminosity dropping by a factor of  $> 5000$  and the UV luminosity decreasing by a factor of  $\sim 15$ . The SED significantly hardens during this transition, similar to the behavior seen in changing-look AGNs and other TDEs. This constitutes the second state transition, after which the source reaches the quiescent state at a low Eddington ratio  $< 0.0004$ .

These transitions between the soft, hard, and quiescent states, as well as the main drivers of disk (in)stabilities in accreting black holes, remain poorly understood, especially so for SMBHs. This work shows that TDEs can provide a unique new opportunity to observationally constrain accretion state properties and transitions in individual SMBHs. In comparison to changing-look AGNs (Gezari et al. 2017b; Frederick et al. 2019; Ruan et al. 2019; Trakhtenbrot et al. 2019), TDEs evolve faster, facilitating coordinated observational studies of the full evolution of accretion cycles and transitions. Furthermore, TDEs are readily discovered at increasing rates in wide-field optical and X-ray photometric surveys without the need for archival observations such as spectroscopy (to determine whether the source has changed state). We have demonstrated that a detailed characterization of both the soft and hard states, as well as transition timescales and changes in the interplay between the different emitting regions, is possible. In summary, TDEs enable direct studies of the apparent scale invariance of accretion processes across seven orders of magnitude in black hole mass. In the future, statistical samples of TDEs with UV and radio monitoring observations, as well as soft and hard X-ray observations covering both short (stare) and long (monitoring) timescales, will allow in-depth comparisons between stellar-mass black hole and SMBH accretion flow properties.

We thank D. J. Walton, W. N. Alston, A. C. Fabian, C. Reynolds, E. Coughlin, K. Hayasaki, and M. I. Saladino for discussions and the anonymous referee for constructive comments and suggestions. We are grateful to the Swift, XMM-Newton, NICER, and Chandra operation teams and PIs for awarding and scheduling the ToO/DDT observations. T.W. was funded in part by European Research Council grant 320360 and by European Commission grant 730980. S.v.V. was supported by the James Arthur Postdoctoral Fellowship. This research was partially supported by the Australian Government through the Australian Research Council’s Discovery Projects funding scheme (project DP200102471). Raw optical/UV/X-ray observations are available in the NASA/Swift archive (<http://heasarc.nasa.gov/docs/swift/archive>; Target Names: AT2018fyk, ASASSN-18UL), the XMM-Newton Science Archive (<http://nxsas.esac.esa.int>; obsIDs: 0831790201, 0853980201, 0854591401), and the Chandra data archive (<https://cxc.harvard.edu/cda/>; obsID: 23289). NICER data are publicly available through the HEASARC: <https://heasarc.gsfc.nasa.gov/cgi-bin/W3Browse/w3browse.pl>.

*Facilities:* XMM-Newton, Swift(XRT and UVOT), NICER, CXO, Magellan, ATCA.

*Software:* astropy (Astropy Collaboration et al. 2013), Heasoft (NASA High Energy Astrophysics Science Archive Research Center (Heasarc), 2014), CIAO (Fruscione et al. 2006), gPHOTON (Million et al. 2016), CASA (McMullin et al. 2007).

### ORCID iDs

T. Wevers  <https://orcid.org/0000-0002-4043-9400>  
 D. R. Pasham  <https://orcid.org/0000-0003-1386-7861>  
 S. van Velzen  <https://orcid.org/0000-0002-3859-8074>  
 J. C. A. Miller-Jones  <https://orcid.org/0000-0003-3124-2814>  
 P. Uttley  <https://orcid.org/0000-0001-9355-961X>  
 K. C. Gendreau  <https://orcid.org/0000-0001-7115-2819>  
 R. Remillard  <https://orcid.org/0000-0003-4815-0481>  
 A. Chiti  <https://orcid.org/0000-0002-7155-679X>

### References

- Abramowicz, M. A., & Fragile, P. C. 2013, *LRR*, 16, 1
- Alexander, K. D., van Velzen, S., Horesh, A., & Zauderer, B. A. 2020, *SSRv*, 216, 81
- Arnaud, K. A. 1996, in ASP Conf. Ser. 101, *Astronomical Data Analysis Software and Systems V*, ed. G. H. Jacoby & J. Barnes (San Francisco, CA: ASP), 17
- Astropy Collaboration, Robitaille, T. P., Tollerud, E. J., et al. 2013, *A&A*, 558, A33
- Calzetti, D., Armus, L., Bohlin, R. C., et al. 2000, *ApJ*, 533, 682
- Cash, W. 1979, *ApJ*, 228, 939
- Conroy, C., Gunn, J. E., & White, M. 2009, *ApJ*, 699, 486
- Corbel, S., & Fender, R. P. 2002, *ApJL*, 573, L35
- Dey, A., Schlegel, D. J., Lang, D., et al. 2019, *AJ*, 157, 168
- Done, C., & Gierliński, M. 2005, *MNRAS*, 364, 208
- Dong, S., Shappee, B. J., Prieto, J. L., et al. 2016, *Sci*, 351, 257
- Dunn, R. J. H., Fender, R. P., Körding, E. G., Belloni, T., & Cabanac, C. 2010, *MNRAS*, 403, 61
- Falcke, H., Körding, E., & Markoff, S. 2004, *A&A*, 414, 895
- Fender, R. P. 2001, *MNRAS*, 322, 31
- Fender, R. P., Belloni, T. M., & Gallo, E. 2004, *MNRAS*, 355, 1105
- Fender, R. P., Gallo, E., & Jonker, P. G. 2003, *MNRAS*, 343, L99
- Frederick, S., Gezari, S., Graham, M. J., et al. 2019, *ApJ*, 883, 31
- French, K. D., Arcavi, I., & Zabludoff, A. 2017, *ApJ*, 835, 176
- Fruscione, A., McDowell, J. C., Allen, G. E., et al. 2006, *Proc. SPIE*, 6270, 62701V
- Gendreau, K. C., Arzoumanian, Z., Adkins, P. W., et al. 2016, *Proc. SPIE*, 9905, 99051H
- Gezari, S., Cenko, S. B., & Arcavi, I. 2017a, *ApJL*, 851, L47
- Gezari, S., Hung, T., Cenko, S. B., et al. 2017b, *ApJ*, 835, 144
- Giustini, M., Miniutti, G., & Saxton, R. D. 2020, *A&A*, 636, L2
- Gliozzi, M., & Williams, J. K. 2020, *MNRAS*, 491, 532
- González-Martín, O., & Vaughan, S. 2012, *A&A*, 544, A80
- Heil, L. M., Uttley, P., & Klein-Wolt, M. 2015, *MNRAS*, 448, 3339
- HI4PI Collaboration, Ben Bekhti, N., Flöer, L., et al. 2016, *A&A*, 594, A116
- Hills, J. G. 1975, *Natur*, 254, 295
- Hinkle, J. T., Holoien, T. W. S., Shappee, B. J., & Auchettl, K. 2021, *ApJ*, 910, 83
- Holoien, T. W. S., Kochanek, C. S., Prieto, J. L., et al. 2016, *MNRAS*, 463, 3813
- Homan, J., & Belloni, T. 2005, *Ap&SS*, 300, 107
- Homan, J., Fridriksson, J. K., Jonker, P. G., et al. 2013, *ApJ*, 775, 9
- Hung, T., Gezari, S., Blagorodnova, N., et al. 2017, *ApJ*, 842, 29
- Jansen, F., Lumb, D., Altieri, B., et al. 2001, *A&A*, 365, L1
- Jonker, P. G., Stone, N. C., Generozov, A., Velzen, S. v., & Metzger, B. 2020, *ApJ*, 889, 166
- Kalemci, E., Dinçer, T., Tomsick, J. A., et al. 2013, *ApJ*, 779, 95
- Kelley, L. Z., Tchekhovskoy, A., & Narayan, R. 2014, *MNRAS*, 445, 3919
- Komossa, S., Halpern, J., Schartel, N., et al. 2004, *ApJL*, 603, L17
- Körding, E., Falcke, H., & Corbel, S. 2006a, *A&A*, 456, 439
- Körding, E. G., Jester, S., & Fender, R. 2006b, *MNRAS*, 372, 1366
- Leloudas, G., Fraser, M., Stone, N. C., et al. 2016, *NatAs*, 1, 0002
- Lightman, A. P., & Eardley, D. M. 1974, *ApJL*, 187, L1
- Lusso, E., Comastri, A., Vignali, C., et al. 2010, *A&A*, 512, A34
- Maccarone, T. J., Gallo, E., & Fender, R. 2003, *MNRAS*, 345, L19
- Maksym, W. P., Lin, D., & Irwin, J. A. 2014, *ApJL*, 792, L29
- Marshall, K. 2015, *ApJ*, 810, 52
- McElroy, R. E., Husemann, B., Croom, S. M., et al. 2016, *A&A*, 593, L8
- McHardy, I. M., Koerding, E., Knigge, C., Uttley, P., & Fender, R. P. 2006, *Natur*, 444, 730
- McMullin, J. P., Waters, B., Schiebel, D., Young, W., & Golap, K. 2007, in ASP Conf. Ser. 376, *Astronomical Data Analysis Software and Systems XVI*, ed. R. A. Shaw, F. Hill, & D. J. Bell (San Francisco, CA: ASP), 127
- Merloni, A., Heinz, S., & di Matteo, T. 2003, *MNRAS*, 345, 1057
- Miller-Jones, J. C. A., Bahramian, A., Orosz, J. A., et al. 2021, *Sci*, 371, 1046
- Million, C., Fleming, S. W., Shiao, B., et al. 2016, *ApJ*, 833, 292
- Miniutti, G., Saxton, R. D., Giustini, M., et al. 2019, *Natur*, 573, 381
- Mockler, B., Guillochon, J., & Ramirez-Ruiz, E. 2019, *ApJ*, 872, 151
- NASA High Energy Astrophysics Science Archive Research Center (Heasarc) 2014, HEASoft: Unified Release of FTOOLS and XANADU v6.24, Astrophysics Source Code Library, ascl:1408.004
- Nikolajuk, M., & Walter, R. 2013, *A&A*, 552, A75
- Noda, H., & Done, C. 2018, *MNRAS*, 480, 3898
- Parker, M. L., Schartel, N., Grupe, D., et al. 2019, *MNRAS*, 483, L88
- Pasham, D. R., & van Velzen, S. 2018, *ApJ*, 856, 1
- Plotkin, R. M., Gallo, E., & Jonker, P. G. 2013, *ApJ*, 773, 59
- Plotkin, R. M., Gallo, E., Markoff, S., et al. 2015, *MNRAS*, 446, 4098
- Plotkin, R. M., Miller-Jones, J. C. A., Gallo, E., et al. 2017, *ApJ*, 834, 104
- Rees, M. J. 1988, *Natur*, 333, 523
- Remillard, R. A., & McClintock, J. E. 2006, *ARA&A*, 44, 49
- Roman, P. W. A., Kennedy, T. E., Mason, K. O., et al. 2005, *SSRv*, 120, 95
- Ruan, J. J., Anderson, S. F., Eracleous, M., et al. 2019, *ApJ*, 883, 76
- Russell, D. M., Miller-Jones, J. C. A., Maccarone, T. J., et al. 2011, *ApJL*, 739, L19
- Shakura, N. I., & Sunyaev, R. A. 1976, *MNRAS*, 175, 613
- Shappee, B. J., Prieto, J. L., Grupe, D., et al. 2014, *ApJ*, 788, 48
- Shen, R.-F., & Matzner, C. D. 2014, *ApJ*, 784, 87
- Shiokawa, H., Krolik, J. H., Cheng, R. M., Piran, T., & Noble, S. C. 2015, *ApJ*, 804, 85
- Sobolewska, M. A., Papadakis, I. E., Done, C., & Malzac, J. 2011a, *MNRAS*, 417, 280
- Sobolewska, M. A., Siemiginowska, A., & Gierliński, M. 2011b, *MNRAS*, 413, 2259
- Stein, R., van Velzen, S., Kowalski, M., et al. 2021, *NatAs*, in press
- Stone, N. C., Kesden, M., Cheng, R. M., & van Velzen, S. 2019, *GRGr*, 51, 30
- Tananbaum, H., Avni, Y., Branduardi, G., et al. 1979, *ApJL*, 234, L9
- Trakhtenbrot, B., Arcavi, I., MacLeod, C. L., et al. 2019, *ApJ*, 883, 94
- Ulmer, A. 1999, *ApJ*, 514, 180
- Uttley, P., McHardy, I. M., & Papadakis, I. E. 2002, *MNRAS*, 332, 231
- Vahdat Motlagh, A., Kalemci, E., & Maccarone, T. J. 2019, *MNRAS*, 485, 2744
- van Velzen, S., Anderson, G. E., Stone, N. C., et al. 2016a, *Sci*, 351, 62
- van Velzen, S., Gezari, S., Hammerstein, E., et al. 2021, *ApJ*, 908, 4
- van Velzen, S., Körding, E., & Falcke, H. 2011, *MNRAS*, 417, L51
- van Velzen, S., Mendez, A. J., Krolik, J. H., & Gorjian, V. 2016b, *ApJ*, 829, 19
- van Velzen, S., Stone, N. C., Metzger, B. D., et al. 2019, *ApJ*, 878, 82
- Vasudevan, R. V., & Fabian, A. C. 2007, *MNRAS*, 381, 1235
- Vaughan, S., Reeves, J., Warwick, R., & Edelson, R. 1999, *MNRAS*, 309, 113
- Wen, S., Jonker, P. G., Stone, N. C., Zabludoff, A. I., & Psaltis, D. 2020, *ApJ*, 897, 80
- Wevers, T. 2020, *MNRAS*, 497, L1
- Wevers, T., Pasham, D. R., van Velzen, S., et al. 2019a, *MNRAS*, 488, 4816
- Wevers, T., Stone, N. C., van Velzen, S., et al. 2019b, *MNRAS*, 487, 4136
- Wevers, T., van Velzen, S., Jonker, P. G., et al. 2017, *MNRAS*, 471, 1694
- Wright, E. L., Eisenhardt, P. R. M., Mainzer, A. K., et al. 2010, *AJ*, 140, 1868
- Yang, Q.-X., Xie, F.-G., Yuan, F., et al. 2015, *MNRAS*, 447, 1692